

Final Technical Report

USGS Award 08HQGR0018

**Hybrid three-dimensional modeling of earthquake  
ground motion in basins, including nonlinear  
wave propagation in soils**

PI: Jacobo Bielak

Computational Seismology Laboratory  
Department of Civil and Environmental Engineering  
Carnegie Mellon University  
Pittsburgh, PA 15213-3890

Office: 123H Porter Hall  
P: 412-268-2958 F: 412-268-7813  
Email: [jbielak@cmu.edu](mailto:jbielak@cmu.edu)

April 30, 2009



## Abstract

Thanks to the continuous growth of computational capabilities and advances in modeling methodologies, seismologists and engineers are now able to simulate strong ground motion at a scale and frequency-level never envisioned before. Most of these simulations, however, continue to be done considering linear soil conditions. Although nonlinear soil behavior was largely debated for decades, its occurrence during moderate to large earthquakes has now been widely acknowledged, especially due to the evidence gathered after events like the Loma Prieta, 1989 and Northridge, 1994 earthquakes. Despite direct observations from earthquakes and in the laboratory, three-dimensional (3D) effects of soil nonlinearity on the spatial and temporal distribution of ground shaking are still far from being well-understood. In fact, its effects are still usually omitted or only treated approximately as part of ground shaking forecasting methods. Under this panorama, the main objective of our research was to develop the capability for modeling ground motion in basins due to moderate to strong earthquakes, taking nonlinear soil behavior into consideration, and to apply and validate this capability to realistic situations. Our plan was to first gain physical insight through simplified problems under idealized conditions regarding both nonlinear soil behavior and 3D basin shapes. This report summarizes the approach and first results of our work toward these objectives. Although we initially envisioned this being done in a hybrid two-step manner, combining our own software for large-scale anelastic earthquake simulations with other commercial software capable of modeling plasticity, we later realized that this approach, despite its advantages, had computational constraints in its efficiency and scalability for our own long-term objectives. This led us to reset the course of action and tackle the problem in a direct manner using and enhancing our own software. We have successfully implemented the necessary tools to represent nonlinear soil behavior by incorporating two basic material models for plasticity and have conducted experiments to test our implementation. In this report we describe our methodology and present results for the simulation of a realistic basin with nonlinear soil conditions subjected to two moderate earthquakes, one immediately below and the other far from the basin. We compare the elastic and inelastic response of the basin and discuss the different contrasting results obtained from considering its nonlinear response.

### Publications resulted from this grant:

Taborda, R. and Bielak, J. (2009). Three-dimensional modeling of earthquake ground motion including nonlinear wave propagation in soils. *Seismological Research Letters*, 80(2):320. SSA Annual Meeting, Monterey, CA, USA, April 8–10.



# Three-dimensional modeling of earthquake ground motion in basins, including nonlinear wave propagation in soils

Ricardo Taborda<sup>1</sup> and Jacobo Bielak<sup>2</sup>

## 1 Introduction

For decades, geotechnical engineers and seismologists debated the existence and relevance of nonlinear soil behavior during earthquakes. Even though laboratory tests showed that under certain conditions the soil would behave nonlinearly, the influence of such behavior on ground motion was not widely acknowledged until relatively recent evidence came to light, mainly during the Loma Prieta, 1989 and Northridge, 1994 earthquakes. Although direct observations and one-dimensional (1D) simulations have shown that strong earthquake ground motion generally decreases as a consequence of nonlinear soil behavior within certain frequency ranges and increases at other frequencies, the three-dimensional (3D) effects of soil nonlinearity on the spatial and temporal distribution of ground shaking are not yet completely understood. In ground shaking forecasting methods and in practice, such effects are often reduced to one- (1D) or two-dimensional (2D) models, if not simply omitted. This has been so because 3D nonlinear earthquake ground motion modeling in basins involve huge and delicate computational challenges of convergence and stability.

The latest developments in computational seismology have not escaped to this situation. During the last decades the continuous growth of computational capabilities and advances in modeling methodologies, have made possible for seismologists and engineers to simulate strong ground motion at a scale and frequency-level never envisioned before. Based on methods developed in the 1960s and perfectionated in the 1970s (Alterman and Karal, 1968; Boore, 1970, 1972; Lysmer and Drake, 1972; Kelly et al., 1976; Archuleta and Day, 1980), full three-dimensional large-scale simulations are making it possible for the scientific community to study the effects of complex rupture processes, directivity, and path and site effects. Among the earliest 3D simulations stands out the work of Frankel and Vidale (1992), who aimed at reproducing the effects of a far-field point source from an aftershock of the 1989 Loma Prieta earthquake in the Santa Clara Valley, California. Most of these simulations were done using finite differences, or other spatial and time discrete representations (e.g. Olsen et al., 1995a,b; Graves, 1996, 1998; Pitarka et al., 1998; Furumura and Koketsu, 2000; Frankel and Stephenson, 2000), low-order finite elements (e.g. Bao et al., 1996, 1998; Tu et al., 2006b), or high-order finite element or spectral element methods (e.g. Seriani and Priolo, 1994; Seriani, 1998; Komatitsch and Vilotte, 1998; Komatitsch et al., 2004; Käser and Dumbser, 2006; Käser and Gallovic, 2008). Among the most recent work we highlight the contribution done with the lead of the Southern California Earthquake Center (SCEC) for the TeraShake and ShakeOut scenario earthquakes (Olsen et al., 2006, 2008, 2009; Graves et al., 2008; Jones et al., 2008). The latter have been thoroughly evaluated by Bielak et al. (2009).

All these simulations were done considering linear soil conditions. In fact, Komatitsch et al. (2004) pointed this out as one possible cause for the differences observed between simulation results and actual event recordings used for validation. This may also be a reason why the results in Olsen et al. (2006) seem rather large compared to those observed in recent large earthquakes. In this work we

---

<sup>1</sup>Ph.D. Candidate, Computational Seismology Laboratory, Department of Civil and Environmental Engineering, A7B Porter Hall, Carnegie Mellon University, Pittsburgh, PA 15213-3890. E-mail: [rtaborda@andrew.cmu.edu](mailto:rtaborda@andrew.cmu.edu).

<sup>2</sup>University Professor, Department of Civil and Environmental Engineering, 123H Porter Hall, Carnegie Mellon University, Pittsburgh, PA 15213-3890. E-mail: [jbielak@cmu.edu](mailto:jbielak@cmu.edu).

aimed at reverting this trend by implementing a simple methodology to allow us to perform fully 3D simulations incorporating nonlinear soil behavior. Based on our own experience in the field (Xu, 1998; Xu et al., 2003), we initially envisioned this being done in a two-step hybrid manner by combining our in-house developed software for large-scale anelastic earthquake simulations (*Hercules*<sup>3</sup>) with a commercial or publicly available software capable of modeling nonlinear soil materials. However, we later realized that this approach represented further complications of computational performance and scalability for regional-size simulations. Thus, we decided to incorporate nonlinear modeling capabilities into *Hercules* itself and approach the problem in a direct manner. In this first work, nonlinearity is implemented by modeling the soil with the von Mises and Drucker-Prager formulations for elastoplastic materials. We have discretized the inelastic wave equations in space using the finite element method, and its evolution in time using central differences. The solution of the resulting semi-discrete nonlinear elastoplastic ordinary differential equations is computed explicitly step-by-step. This has allowed us to come up with an efficient simulation code that inherits the computational capabilities of *Hercules* (an end-to-end approach with integrated rapid mesh generation, numerical efficiency, and highly scalable in large next-generation supercomputers).

In this report we briefly review the history of nonlinear soil in seismology and engineering, set the bases relevant to our implementation from the theory of plasticity, and describe our simulation methodology. We then present an application of our implementation for the study of a realistic basin with nonlinear soil characteristics subjected to two different earthquake scenarios originated in the near and far field. We compare the results of the elastic and inelastic response of the basin for both cases from a regional and local perspective. The comparisons reveal the importance of considering nonlinear soil conditions and gives relevant insights about the influence of three-dimensionality for the problem of spatial and amplitude variability. Our work ultimately aims at fully incorporating nonlinearity into large-scale earthquake simulations and urban seismology, which to date do not yet consider this important aspect in 3D strong ground motion modeling and analysis.

## 2 Nonlinear Soil in Seismology and Engineering

The most common manifestations of inelastic soil behavior under increasing load are (1) a reduction in shear wave velocity and (2) an increase in soil attenuation (Hardin and Drnevich, 1972). Nevertheless, for a long time, strong motion seismologists did not devote significant research attention to the nonlinear phenomena. Though it was known to geotechnical engineers since early on (Seed and Idriss, 1969), it appeared to seismologists that soil responses being observed during earthquakes were satisfactorily explained by other considerations. It might actually be possible that, during a considerable period of time, the seismological community overlooked the presence of nonlinearities (Beresnev and Wen, 1996). Mainly due to the absence of sufficient and reliable data, explanations of soil nonlinearity at sites, other than those involving liquefaction, were for some time regarded as a dubious proposition.

The growing number of available accelerograms and the better characterization of sites changed this perspective (Aki, 2003). In the last two decades, evidence of nonlinear soil response has been slowly accumulating. One of the first cases to provide reliable records of events for the study of nonlinear site effects were the downhole accelerograph arrays of Taiwan, SMART1 and SMART2 (Abrahamson et al., 1987). The analysis of their recordings revealed significant nonlinear soil response, manifested in deamplification of the motion and reduction of shear wave velocities for peak ground accelerations larger than 0.15 g (Chang et al., 1989; Wen, 1994; Beresnev, 1995). The 1989 Loma Prieta earthquake in California presented another case in which nonlinear site effects were captured (Chin and Aki, 1991; Darragh and Shakal, 1991; Beresnev, 2002; Rubinstein and Beroza, 2004a,b; Schaff and Beroza, 2004). Chin and Aki (1991) studied nonlinear effects at sediment sites in the epicentral region by eliminating

---

<sup>3</sup>*Hercules* is an octree-based finite element parallel software for the simulation of ground motion due to earthquakes generated by kinematic faulting developed by the Quake group at Carnegie Mellon (Tu et al., 2006a,b)

the influences of radiation pattern and topography, concluding that nonlinear effects occurred at levels above 0.1-0.3 g. Beresnev (2002) compared linear simulations to recorded data and found differences attributable to soil nonlinearities in the range of 1-3Hz. Rubinstein and Beroza (2004a,b) and Schaff and Beroza (2004) studied the changes in shear wave velocities and detected delays revealing the presence of nonlinear behavior. Darragh and Shakal (1991) estimated the response of a soil site by studying the ratio of smoothed Fourier amplitude spectra from a soil site and a nearby rock site, and observed strong motion deamplification effects. Following the 1994 Northridge earthquake, more plausible evidence of nonlinear effects was brought to the attention of the engineering and seismological community (Bardet and Davis, 1996; Trifunac and Todorovska, 1996; Field et al., 1997). Trifunac and Todorovska (1996) analyzed the observed strong motion amplitudes in the San Fernando valley and found that noticeable reduction in recorded horizontal peak accelerations occur at sites with shear wave velocities less than 360 m/s and distances from the fault less than 15-20 km. Field et al. (1997) compared the mainshock to the aftershocks and reported sediment deamplification up to a factor of two. This implied significant nonlinearities. More recently, others have studied the potential effect of nonlinear soil behavior in the area of Seattle (Hartzell et al., 2002; Frankel et al., 2002), and have concluded that nonlinear soil effects could have a significant impact. This kind of studies also have been conducted in Japan (e.g. Satoh et al., 1995; Tsuda et al., 2006; Rubinstein et al., 2007). They have come to similar conclusions.

Simulations of nonlinear earthquake response in geotechnical engineering began in the late 1960s. These early studies were conducted for horizontally layered soils and vertically incident waves, by either an equivalent linear or a direct nonlinear method. Many studies have concluded that equivalent linear methods cannot reproduce some of the important characteristics of the seismic ground motion, especially for the case of strong loadings (Streeter et al., 1974; Finn et al., 1978). This is because equivalent linear methods overestimate the seismic response due to pseudo-resonance at periods corresponding to the strain-compatible stiffness used in the final elastic iteration analysis. Also, since the method is elastic it cannot predict the permanent deformations that occur during an earthquake. These are of high importance for assessing the damage in long structures and structures susceptible to differential ground motions such as bridges. By contrast, the direct nonlinear method can reproduce these characteristics since the shear modulus is modified at every time step according to the current strain. Thus, the nonlinear stress-strain relationship is closely followed. A number of representations have been used for the backbone curves and yield rules of soil stress-strain relationship. They include, e.g. linear (Idriss and Seed, 1968), multilinear (Joyner, 1975; Yu et al., 1993) and one by (Archuleta et al., 2000) based on a modified Masing rule with a provision for pore pressure (Elgamal, 1991). Although from the plasticity point of view, there is a wide variety of models that apply different yield criteria, flow rules, and hardening laws with a broad range of complexity, simulations continue to predominantly incorporate nonlinearity making use of 1D models. One could argue that the use of 1D models has been in some sense abused, because, while they can yield reasonable estimates of nonlinear effects under vertically incident seismic excitation, they cannot represent the effects of surface waves and basin effects. A good example of how 1D simulations have been considered into synthetic realizations is the work by Archuleta et al. (2003) in which nonlinearity was introduced into the calculation at the final stage of a stochastic procedure for the vertically propagating waves from the basement to the surface. The few 2D and  $2\frac{1}{2}$ D studies to date of nonlinear soil amplification (e.g. Joyner, 1975; Joyner and Chen, 1975; Elgamal, 1991; Marsh et al., 1995; Zhang and Papageorgiou, 1996), though they have confirmed the importance of nonlinearity on site response, still cannot assure that a complete three dimensional approach would not bring more information to the interpretation of results. In particular, a  $2\frac{1}{2}$ D study of the Marina District in San Francisco during the 1989 Loma Prieta earthquake found that the focusing and lateral interferences often observed in studies based on linear soil behavior are still present for strong excitation though not as prominently as for weak excitation (Zhang and Papageorgiou, 1996). The use of an equivalent linearization technique meant that no permanent deformations could be detected.

Three-dimensional simulations of nonlinear effects have not been entirely absent, but due to their complexity, their use has been limited to the study of special structures such as bridges, dams, or nuclear power plants. A good example of this is the research done on the dynamic response of the Humboldt Bay Middle Channel Bridge, its foundation system, and the ground around it (Zhang et al., 2003, 2004, 2008; Elgamal et al., 2008; Yang et al., 2003; Yan, 2006). In this series of papers, the authors used complex nonlinear soil models with multi-yielding surfaces to study the seismic response of the bridge. They considered 2D and 3D models and, although the focus was in the structural response of the bridge itself, there were interesting conclusions on the implications of the soil nonlinearity. These and other simulations, however, are of a smaller scale ( $< 1$  km) than that required for the study of regional seismic response. To our knowledge, the only fully 3D simulation aimed at addressing the problem from a regional perspective has been the work of Xu (1998) and Xu et al. (2003). In particular, Xu et al. (2003) used a finite element methodology including inelastic behavior of the soil, due to vertically-incident SH-seismic excitation to study the response of an idealized basin. The soil within the basin was idealized as a Drucker-Prager elastoplastic material (Drucker and Prager, 1952). Their results showed that whereas the ground motion decreases due to soil nonlinearity, the spatial variation of the surface motion followed that of the linear model, having clear basin effects. The main effect of the elastoplastic behavior on the accelerations was to reduce the amplitude of the maximum response by about a factor of 2 in the deepest regions of the basin, where the shear strains were the largest. Despite the significant reduction in peak response and permanent deformations, Xu et al. did not observe a significant change in the basin frequencies.

### 3 Theory of Plasticity

In this section we review some of the basic concepts of plasticity that are relevant to our implementation of nonlinear soil modeling. A more in depth review may be found in the literature (e.g. Fung, 1965; Desai and Christian, 1977; Chen and Han, 1988).

There exist several different nonlinear constitutive models that describe the stress-strain relationships in geomaterials. They depend on many factors, including the homogeneity, isotropy, and continuity of their formulations. In soil mechanics, the predominant approaches for nonlinear behavior are based on Hooke's law of elasticity, where changes in the stress-strain relationships may be introduced in different ways. Elasticity models are relatively simple and yield good results for moderate nonlinear behavior under monotonically increasing loading and static or pseudo-static conditions. And, although some of them may allow hysteretical behavior, they are not the best option for dynamic loading. In such case, flow theory of plasticity is a better extension to the classical stress-strain relationships from Hooke's law and its incremental formulation makes it easier for its implementation in computer codes for finite element analysis.

We use flow theory in our implementation. Flow theory is composed of three basic concepts: the existence of a yield surface that differentiates the elastic and plastic domains, an appropriate hardening law that defines the change, if any, in the yield surface under subsequent loading, and a flow rule that defines the incremental relationship between the plastic strain and the state of stresses as given by a plastic potential function.

#### 3.1 Elastic limit and yield function

A material may be understood as having undergone plastic behavior once it reaches an elastic limit,  $k$ , beyond which elasticity no longer holds. This elastic limit defines a yielding function  $f(\sigma_{ij})$  in term of stress  $\sigma_{ij}$  and may be written as



$$f(\sigma_{ij}) = F(\sigma_{ij}) - k = 0 \quad (1)$$

Equation 1 implies that there exists a yield surface defined by

$$F(\sigma_{ij}) = k \quad (2)$$

where  $k$  may also be understood as a hardening function that defines the position of the yield surface. If  $k$  is constant we say that there is no hardening and our model is perfectly plastic. We will consider  $k$  as constant in our implementation.

### 3.2 Plastic Potential, Flow Rule, and Plastic Multiplier

The yielding function implies that plastic flow only occurs when the material is in a stress state such that the stress point remains on the yield surface. When this occurs we need a relationship between the given stresses and the change in strains while the material remains plastic. That is, a relation between the change in plastic strain and stresses. Such relation is called a flow rule and may be expressed by

$$d\epsilon_{ij}^p = d\lambda \frac{\partial g}{\partial \sigma_{ij}} \quad (3)$$

where  $d\lambda$  is a positive scalar called plastic multiplier. Since plastic flow only occurs when a stress point remains on the yield surface,  $d\lambda$ , and therefore  $d\epsilon_{ij}^p$ , is nonzero only when plasticity occurs and zero otherwise.  $g(\sigma_{ij})$  is a scalar function that defines a plastic potential whose concept was introduced by von Mises in 1928. Equation 3 is important because it describes the behavior of the plastic flow vector,  $d\epsilon_{ij}^p$ , which in turn describes the plastic flow itself, i.e., the behavior of the material once it has reached and remains in the plastic domain.

A special case of flow theory is that of the yield function coinciding with the plastic potential ( $f = g$ ). In this case we call it associated flow rule and write it as follows.

$$d\epsilon_{ij}^p = d\lambda \frac{\partial f}{\partial \sigma_{ij}} \quad (4)$$

In our implementation we will assume the flow rule to be associated to the plastic potential.

### 3.3 Incremental Stress-Strain Relationships

Because the plastic strain is unlimited under plastic flow, it is necessary to formulate the strain in terms of infinitesimal changes or increments,  $d\epsilon_{ij}$ . If we assume that the total strain at a given state can be expressed as the sum of an elastic and a plastic strain tensor, its increment may be written as a sum of these parts as well.

$$d\epsilon_{ij} = d\epsilon_{ij}^e + d\epsilon_{ij}^p \quad (5)$$

From Hooke's law we know that the elastic component of strains relates to the stresses by

$$d\epsilon_{ij}^e = D_{ijkl} d\sigma_{kl} \quad (6)$$

where  $D_{ijkl}$  is the compliance tensor, or the inverse of the material elastic constant tensor,  $C_{ijkl}$ , or

$$d\epsilon_{ij}^e = \frac{dI_1}{9K} \delta_{ij} + \frac{ds_{ij}}{2G} \quad (7)$$

where  $K$  and  $G$  are the bulk and shear modulus, respectively.  $I_1$  is the first invariant of stresses,  $s_{ij}$  is the stress deviatoric tensor, and  $\delta_{ij}$  is the Kronecker delta. In turn, the plastic part is defined by the flow rule given in Eq. 4. Therefore, the complete strain-stress incremental relationship for an elastic-perfectly plastic material may be written as

$$d\epsilon_{ij} = \frac{dI_1}{9K} \delta_{ij} + \frac{ds_{ij}}{2G} + d\lambda \frac{\partial f}{\partial \sigma_{ij}} \quad (8)$$

From the flow rule, we know that  $d\lambda$  is nonzero only when a stress point remains on the yield surface, we say that

$$d\lambda \begin{cases} = 0 & \text{wherever } f < 0 \quad \text{or} \quad f = 0 \text{ but } df < 0 \\ > 0 & \text{wherever } f = 0 \quad \text{and} \quad df = 0 \end{cases} \quad (9)$$

The actual value of  $d\lambda$  is determined by combining the stress-strain relations with a consistency condition. Its complete derivation may be found in Chen and Han (1988). The final result is

$$d\lambda = \frac{3K d\epsilon_{kk} \left( \frac{\partial f}{\partial I_1} \right) + \left( \frac{G}{\sqrt{J_2}} \right) \left( \frac{\partial f}{\partial \sqrt{J_2}} \right) s_{mn} de_{mn}}{9K \left( \frac{\partial f}{\partial I_1} \right)^2 + G \left( \frac{\partial f}{\partial \sqrt{J_2}} \right)^2} \quad (10)$$

where  $J_2$  is the second invariant of the deviatoric stress and  $de$  is the strain deviatoric.

At this point it is clear that for a given yield function  $f(\sigma_{ij})$ , Eqs. 8–10 provide all that is needed to describe the plastic behavior of a given material.

### 3.4 Material Models

For our implementation we have selected two different material models. They are the von Mises and the Drucker-Prager yield criteria. Both models are well understood in the literature and together with the Tresca and Mohr-Coulomb constitute yielding criteria of pressure-dependent materials. Although it is desirable to have more complex and realistic models for soil materials, we have chosen these two models because they are easily related to soil properties (cohesion and friction angle) and because they are easier to implement and test in an initial effort.

#### 3.4.1 von Mises

Formulated in 1913, the von Mises yield criterion is a smooth version of the Tresca yield function that accounts for the influence intermediate principal stresses. In simple terms, it states that plastic flow occurs when the octahedral shearing stress reaches an elastic limit  $k$ . Figure 1a shows the shape of the von Mises yield surface in the principal stresses space. The yield function is of the form

$$f(J_2) = J_2 - k^2 = 0 \quad (11)$$

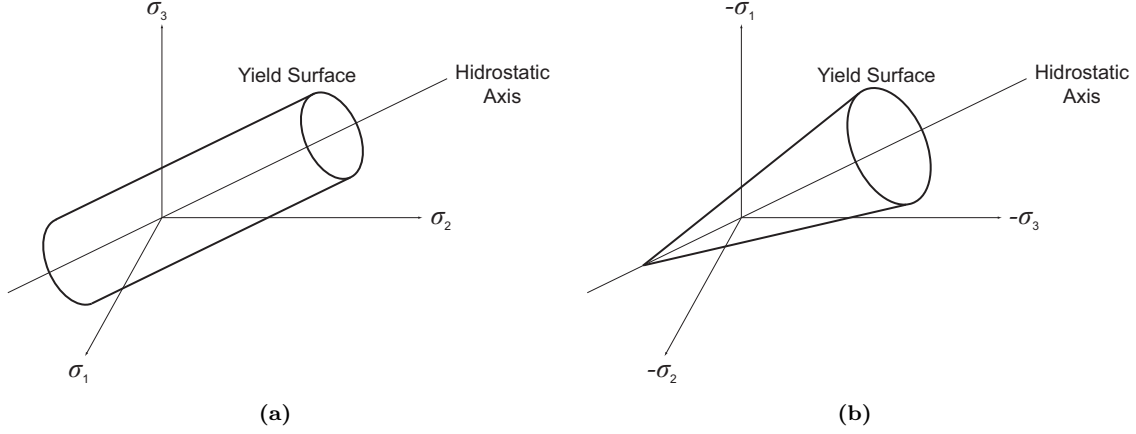


**Figure 1:** Yield surfaces of the (a) von Mises and (b) Drucker-Prager yield criteria.

The value of  $k$  corresponds to the yield stress of the material when subjected to pure shear. Substituting Eq. 11 into 10 yields the following expression for the plastic multiplier.

$$d\lambda = \frac{s_{mn}de_{mn}}{\sqrt{J_2}} \quad (12)$$

### 3.4.2 Drucker-Prager

The Drucker-Prager yield criterion was introduced in 1952 as a modification of the von Mises model. This model incorporates the influence of the normal or hydrostatic stresses into the yield criterion by including an additional term dependent on the angle of friction of the material that scales the first invariant of stresses. It is given by

$$f(I_1, J_2) = \alpha I_1 + \sqrt{J_2} - k = 0 \quad (13)$$

where  $\alpha$  and  $k$  are material constants. In the principal stresses space, the Drucker-Prager yield surface represents a cone that circumscribes the Tresca hexagon when the constants  $\alpha$  and  $k$  are given by

$$\alpha = \frac{2 \sin \phi}{\sqrt{3} (3 - \sin \phi)} \quad (14)$$

$$k = \frac{6c \cos \phi}{\sqrt{3} (3 - \sin \phi)} \quad (15)$$

where  $c$  is the cohesion and  $\phi$  is the angle of internal friction of the material. Substituting Eq. 13 into 10 yields the following expression for the plastic multiplier.

$$d\lambda = \frac{3\alpha K d\epsilon_{kk} + \left(\frac{G}{\sqrt{J_2}}\right) s_{mn}de_{mn}}{9\alpha^2 K + G} \quad (16)$$

Notice that when the material is frictionless, i.e.,  $\phi = 0$ , the constant  $\alpha$  vanishes and the yield function becomes that of the von Mises criterion. The shape of the Drucker-Prager yield surface is shown in Fig. 1b.

## 4 Simulation Methodology

### 4.1 Theoretical Formulation

We start from the linear momentum equation

$$\frac{\partial \tau_{ij}}{\partial x_i} + f_i = \rho \frac{\partial^2 u_i}{\partial t^2} \quad (17)$$

and apply the Galerkin method to later convert the continuous differential equation into an equivalent discrete form. Pursuing such approach yields the following weak form of the equation

$$\int_{\Omega} \rho v_i \frac{\partial^2 u_i}{\partial t^2} d\Omega + \int_{\Omega} \frac{\partial v_i}{\partial x_j} \tau_{ij} d\Omega = \int_{\Omega} \partial v_i f_i d\Omega + \int_{\Gamma} \partial v_i \tau_{ij} n_j d\Gamma \quad (18)$$

where the rightmost term represents the boundary conditions.

On the other hand, we have already seen that the total strain may be written as the sum of the elastic and plastic strains.

$$\begin{aligned} \epsilon_{ij} &= \epsilon_{ij}^e + \epsilon_{ij}^p \\ \epsilon_{ij}^e &= \epsilon_{ij} - \epsilon_{ij}^p \end{aligned} \quad (19)$$

And from Hooke's law

$$\begin{aligned} \tau_{ij} &= C_{ijmn} \epsilon_{mn}^e \\ \tau_{ij} &= C_{ijmn} (\epsilon_{mn} - \epsilon_{mn}^p) \end{aligned} \quad (20)$$

Substituting (20) into (18) and dropping the boundary conditions term one obtains

$$\int_{\Omega} \rho v_i \frac{\partial^2 u_i}{\partial t^2} d\Omega + \int_{\Omega} \frac{\partial v_i}{\partial x_j} C_{ijmn} (\epsilon_{mn} - \epsilon_{mn}^p) d\Omega = \int_{\Omega} \partial v_i f_i d\Omega \quad (21)$$

which can be rearranged as

$$\int_{\Omega} \rho v_i \frac{\partial^2 u_i}{\partial t^2} d\Omega + \int_{\Omega} \frac{\partial v_i}{\partial x_j} C_{ijmn} \epsilon_{mn} d\Omega = \int_{\Omega} \frac{\partial v_i}{\partial x_j} C_{ijmn} \epsilon_{mn}^p d\Omega + \int_{\Omega} \partial v_i f_i d\Omega \quad (22)$$

Because Hooke's law still holds for each of the separate terms in Eq. 20, one can express the product of the material elastic constant tensor with the total component of strains on the second term as a stress tensor  $\sigma_{ij}$ , and do the same for the plastic component on the right hand side,  $\sigma_{ij}^p$ , the weak formulation becomes

$$\int_{\Omega} \rho v_i \frac{\partial^2 u_i}{\partial t^2} d\Omega + \int_{\Omega} \frac{\partial v_i}{\partial x_j} \sigma_{ij} d\Omega = \int_{\Omega} \frac{\partial v_i}{\partial x_j} \sigma_{ij}^p d\Omega + \int_{\Omega} \partial v_i f_i d\Omega \quad (23)$$

This rearrangement, as we will see, implies that we will continue to build the stiffness matrix of the system on the left hand side of Eq. 23 and use the plastic term as a 'corrective' force on the right hand side. This is not done in most applications of plasticity because one does not necessarily need

to construct the element stiffness matrix due to the fact that its calculation is naturally embedded in the calculation of the total stresses (or strains) without need for separating it in their elastic and plastic components. We wanted to preserve the construction of the stiffness matrix because it comes advantageous to our simulations under purely elastic conditions.

We introduce finite elements for spatial discretization of the trial function  $v_i$  and the displacements  $u_i$  by defining

$$v^m = \sum_{m=1}^M \phi^m v_i^m \quad (24)$$

$$u^n = \sum_{n=1}^N \phi^n u_i^n \quad (25)$$

Substituting Eqs. 24 and 24 into 23 and switching the formulation from the global to the element level (where  $\phi$  becomes  $\psi$ ), it is possible to obtain

$$\mathbf{M}\ddot{\mathbf{u}} + \mathbf{K}\mathbf{u} = \sum_e \int_{\Omega_e} \nabla \psi_j \sigma_{ij}^p d\Omega_e + \mathbf{f} \quad (26)$$

where  $\mathbf{M}$  and  $\mathbf{K}$  are the assembled element mass and stiffness matrices, and  $\mathbf{f}$  is the assembled vector of body forces which in the seismic problem is prescribed by the definition of the source rupture for those elements on the fault.  $\ddot{\mathbf{u}}$  and  $\mathbf{u}$  are the vectors of acceleration and displacements. The corresponding element mass and stiffness matrices  $\mathbf{M}_e$  and  $\mathbf{K}_e$  and the load vector  $\mathbf{f}_e$  are given by

$$\mathbf{M}_e = \int_{\Omega_e} \rho \nabla \psi_i \nabla \psi_j \mathbf{I} d\Omega_e \quad (27)$$

$$\mathbf{K}_e = \int_{\Omega_e} \lambda \nabla \psi_i \nabla \psi_j^T \mathbf{I} d\Omega_e + \int_{\Omega_e} \mu (\nabla \psi_i \nabla \psi_j^T + \nabla \psi_i^T \nabla \psi_j \mathbf{I}) d\Omega_e \quad (28)$$

and

$$\mathbf{f}_e = \int_{\Omega_e} \psi_i f d\Omega_e \quad (29)$$

When the integral term in Eq. 26 is not present, we simply have the finite element formulation for the elastic linear problem. Therefore, this terms acts as a ‘corrector’ for plasticity. Formulating the problem on this form allows us to preserve the original implementation on *Hercules*. Moreover, it allows us to introduce an additional term to account for intrinsic attenuation as follows

$$\mathbf{M}\ddot{\mathbf{u}} + \mathbf{C}\dot{\mathbf{u}} + \mathbf{K}\mathbf{u} = \sum_e \int_{\Omega_e} \nabla \psi_j \sigma_{ij}^p d\Omega_e + \mathbf{f} \quad (30)$$

where  $\mathbf{C}$  is the assembled attenuation matrix that for the case of Rayleigh damping may be written as a linear combination of the mass and stiffness matrices. The corresponding element attenuation matrix,  $\mathbf{C}_e$ , is given by

$$\mathbf{C}_e = \alpha_1 \mathbf{M}_e + \alpha_2 \mathbf{K}_e \quad (31)$$

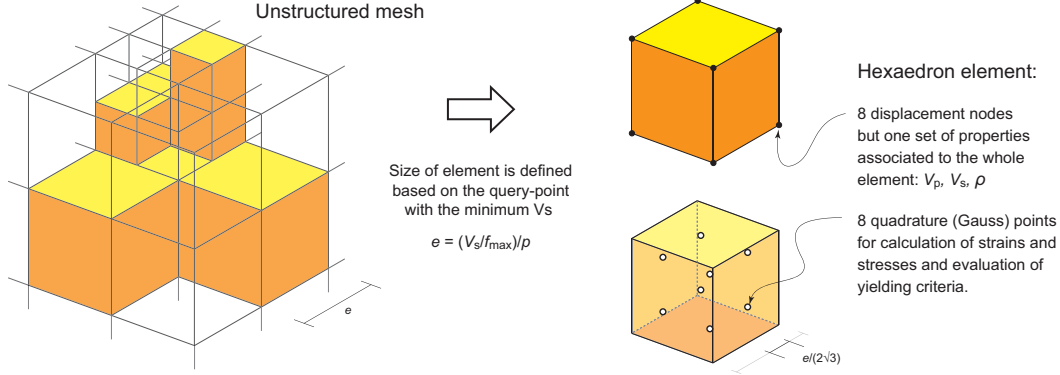


**Figure 2:** Hercules unstructured mesh and typical hexahedron element with displacement nodes and stress/strain quadrature points.

and  $\dot{\mathbf{u}}$  is the vector of nodal velocities. Transforming Eq. 30 into a difference equation using central differences for the acceleration and backwards central differences for velocity, yields

$$\mathbf{M} \left( \frac{\mathbf{u}_{n-1} - 2\mathbf{u}_n + \mathbf{u}_{n+1}}{\Delta t^2} \right) + \mathbf{C} \left( \frac{\mathbf{u}_n - \mathbf{u}_{n-1}}{\Delta t} \right) + \mathbf{K}\mathbf{u}_n = \left( \sum_e \int_{\Omega_e} \nabla \psi_j \sigma_{ij}^p d\Omega_e \right)_n + \mathbf{f}_n \quad (32)$$

where  $\Delta t$  represents the time step and  $n$  represents a given step at time  $t = n\Delta t$ . One can solve Eq. 32 for the forward vector of displacements and obtain

$$\mathbf{u}_{n+1} = \mathbf{M}^{-1} \left[ \left( \sum_e \int_{\Omega_e} \nabla \psi_j \sigma_{ij}^p d\Omega_e \right)_n + \mathbf{f}_n \Delta t^2 - (\mathbf{K} \Delta t^2 + \mathbf{C} \Delta t - 2\mathbf{M}) \mathbf{u}_n - (\mathbf{M} - \mathbf{C} \Delta t) \mathbf{u}_{n-1} \right] \quad (33)$$

which represents the marching forward in time for the displacements. It is noteworthy that the inverse of the mass matrix in the right hand side of Eq. 33 does not pose any computational burden as in our implementation the mass of each element is lumped at its nodes, thus making  $\mathbf{M}$  a diagonal matrix whose inversion is trivial.

## 4.2 Computational Implementation

As mentioned above, *Hercules* is a simulation finite-element parallel code that relies on a linear octree-based mesher and solves the elastic wave equations by approximating the spatial variability of the displacements and the time evolution with tri-linear elements and central differences, respectively. The resulting scheme has a quadratic convergence rate, in both time and space. Elements are cubes with eight displacement nodes at its vertices and their properties are trivially scalable based on their edge size,  $e$ . For the calculation of strains and stresses necessary for the formulation described above for plasticity, eight quadrature or Gaussian points are considered. These points are located at  $e/2\sqrt{3}$  from the center of the element in each direction. Figure 2 shows a simple mesh representation and its typical element characteristics.

*Hercules* partitions the domain by recursively subdividing it into eight cubes (called octants) depending on the targeted S-wavelengths ( $V_s$ ). The final edge-size of an octant must satisfy the meshing rule

$$e \leq \frac{V_s}{pf_{\max}} \quad (34)$$

where  $p$  represents the desired number of points per wavelength and  $f_{\max}$  is the maximum frequency of the simulation. This produces a nonconforming set of elements and nodes. The continuity of the displacements field is enforced by constraining linearly the motion of hanging nodes to anchored or independent ones. Given that the elements share a scaled equivalent geometry, there is no need to store individual element mass and stiffness matrices. This allows to scale the stiffness and lumped-mass matrix-templates according to the material properties and octant edge-size (Kim et al., 2003; Tu et al., 2006a).

The code uses a plane wave approximation of the absorbing boundary condition (Lysmer and Kuhlemeyer, 1969), and introduces a Rayleigh attenuation mechanism in the bulk as described in the previous section. The traction-free boundary conditions at the free-surface are natural in finite elements. Thus, no special treatment is required (Bao et al., 1998). Once the mesh is distributed among the processors, the code obtains the equivalent time dependent forces of the double couples used to represent the source and proceeds to the displacements computation which are obtained in an element-by-element fashion following Eq. 33. This approach allows *Hercules* to considerably reduce memory requirements as compared to standard finite element implementations and makes it much more efficient than the more popular finite differences approach.

With the formulation just described, the computational implementation of nonlinear soil conditions within *Hercules*' simulation scheme is reduced to the determination of the integral term in the right hand side of Eq. 33. Figure 3 describes the algorithm followed in the code.

## 5 Simulation Case Study

We have been part of several research initiatives for large-scale earthquake simulations. Although we have conducted some simulations for other regions of seismological interest (Bielak et al., 1999; Ramírez-Guzmán et al., 2008), most of our efforts have been focused on the simulation of the regional response of southern California (Taborda et al., 2006, 2007; Bielak et al., 2009). Based on that experience we initially set our application objective to be the simulation of a case considering nonlinear soil conditions in the greater Los Angeles basin for a scenario earthquake of characteristics similar to those of the Northridge, 1994 earthquake. However, the complexity in the current material models of this region posed difficulties in selecting and tuning the necessary soil parameters for a nonlinear simulation. Therefore, we decided to change the simulation case study into one that while still representing a realistic basin of interest, it would be easier to control the soil simulation parameters. We happened to be working in collaboration with a European group studying the seismic response of the region of Tessoniki in Greece and found this an interesting case for a nonlinear simulation.

### 5.1 The Euroseistest Numerical Benchmark

In 2008 several research groups gathered to define a numerical benchmark to conduct different numerical simulations for the Euroseistest to thoroughly verify the different numerical methods on well-defined test cases (Bard et al., 2008). Phase I of this effort included a 3D simulation of an area of about 16 km x 29 km subjected to a hypothetical earthquake with epicenter just beneath the pass between the basins of the Volvi and Langada lakes in the Mygdonian graben. This region has been studied extensively, and therefore, its geometry and mechanical properties are relatively well-constrained. We built upon and modified the benchmark case to study the effect that nonlinear soil conditions may have in the response of the valley due to two point sources in the near- and far-field.

Known quantities at the beginning of time-step n:

$$\mathbf{u}_{n-1}, \mathbf{u}_n, \sigma_{n-1}, \sigma_{n-1}^p, f(\sigma)_{n-1}$$

Solution of plastic quantities:

1.  $d\mathbf{u}_n = \mathbf{u}_n - \mathbf{u}_{n-1}$
2.  $d\epsilon_n = \frac{1}{2} (\nabla \psi_j d\mathbf{u}_n + \nabla \psi_j^T d\mathbf{u})$
3.  $d\sigma_n = 2G d\epsilon + K d\epsilon \mathbf{I}$
4.  $\sigma_n = \sigma_{n-1} + d\sigma_n$
5. Calculate stress invariants  $I_{1n}$  and  $J_{2n}$
6.  $F(\sigma)_n = \alpha I_{1n} + \sqrt{J_{2n}}$
7.  $f(\sigma)_n = F(\sigma)_n - k$
8.  $df(\sigma)_n = f(\sigma)_n - f(\sigma)_{n-1}$
9. If  $(f < 0)$  or  $(f = 0 \text{ and } df < 0)$   
 $d\lambda = 0$
10. If  $(f = 0)$  and  $(df = 0)$   
 $d\lambda \neq 0$
11.  $d\sigma_n^p = d\lambda \left( \frac{G}{\sqrt{J_{2n}}} s + 3\alpha K \mathbf{I} \right)$

Update of stresses at time-step n:

$$\sigma_n^p = \sigma_{n-1}^p + d\sigma_n^p$$

$$\sigma_n = \sigma_{n-1} + d\sigma_n - d\sigma_n^p$$

Solve the displacement field at time-step n+1:

$$\mathbf{u}_{n+1} = \mathbf{M}^{-1} \left[ \left( \sum_e \int_{\Omega_e} \nabla \psi_j \sigma_n^p d\Omega_e \right) + \mathbf{f}_n \Delta t^2 - (\mathbf{K} \Delta t^2 + \mathbf{C} \Delta t - 2\mathbf{M}) \mathbf{u}_n - (\mathbf{M} - \mathbf{C} \Delta t) \mathbf{u}_{n-1} \right]$$

**Figure 3:** Algorithm implemented in *Hercules* to account for the effects of plasticity. The equations are written for the more general case of a Drucker-Prager material model.

## 5.2 Region and Material Model

Figure 4 shows the region of Thessaloniki—an extensively studied, earthquake-prone region in northern Greece—the location of the Euroseistest, and the horizontal projection of the modeling domain. A description of the seismological conditions of the region and the most relevant studies for the area may be found in the literature (e.g. Raptakis et al., 1998; Semblat et al., 2005; Raptakis et al., 2000). The modeling domain is shown in greater detail in Fig. 5, which also includes the location of the sources and indicates three recording locations (stations S1, S2, and S3) which we will use for future reference, and three vertical cross sections of interest. These cross sections may be seen in Fig. 6. The original model used in the benchmark was based upon the information described in Pitilakis (2008) and Papazachos (1998). It consisted of three soft layers (with  $V_{s\min} = 200$  m/s) on top of a horizontally layered bedrock with  $V_s$  values starting at 2600 m/s at 500 m depth, and increasing with depth up to 4400 m/s at 39 km depth. We extended the bottom layer of the domain to 41 km and omitted the uppermost softest layer in the basin for modeling convenience. The basin properties are given in Fig. 6 and Table 1 presents the properties for the strata outside the basin. Anelastic attenuation was modeled using a prescribed relationship between the quality factor  $Q$  and the seismic velocity  $V_s$  at the element level using a global value of  $Q = 50V_s$ . The coefficients  $\alpha_1$  and  $\alpha_2$  in Eq. 31



are determined from  $1/Q(\omega) = \alpha_1/\omega + \alpha_2\omega$  using least squares over a selected bandwidth  $(\omega_1, \omega_2)$ , in order to minimize the difference of  $1/Q(\omega)$  with respect to the constant target value  $1/Q = (50V_s)^{-1}$  over the simulation bandwidth (Bielak et al., 1999).

With regard to plastic behavior, we only allowed the deposits within the basin to behave nonlinearly, forcing all material outside the basing to remain elastic. The soil in the basin was considered to be a frictionless material thus the material model used in the simulation was that of von Mises. To ensure the occurrence of plastic behavior, the soil elastic limits were set to fictitious values of about 1/3 of the maximum pure shear stress under elastic conditions. Values of  $k$  for the N- and F-source cases for each type of soil in the basin are shown in Fig. 6.

### 5.3 Source Definitions

We consider two different cases of excitation, the first one right beneath the basin at 5 km depth and a second one far from the valley and at just 1 km depth. We will refer to them as the N- and F-source events, respectively. Both are point sources modeled as double-couples that generate earthquakes of magnitudes  $M_w = 5.3$  and 5.2. Their localization coordinates and general characteristics are given in Table 2 and graphically in the right part of Fig. 5. Figure 7 shows the normalized slip, and the slip rate with its corresponding Fourier amplitude spectrum. This slip function is the same as that defined for the Euroseistest benchmark but has been refiltered at 1Hz (lowpass). The final slip and area of rupture have been appropriately scaled to generate the given magnitudes.

### 5.4 Simulation Parameters

Table 3 summarizes the simulation parameters and input data used for the simulations. Notice that although the corner frequency of the slip function is 1 Hz we constructed the mesh to be accurate for up to 2 Hz. This is important because plastic flow causes the discrete system to become nonlinear and introduces oscillations of higher frequencies than that of the excitation. In fact, this phenomenon is a possible source of instability in the system that may be controlled in part by building finer meshes or using smaller time steps.

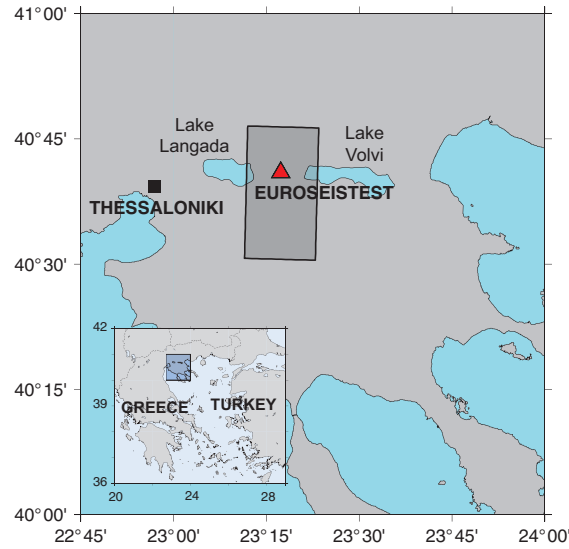


**Figure 4:** Location of the Euroseistest and horizontal projection of the modeling area.

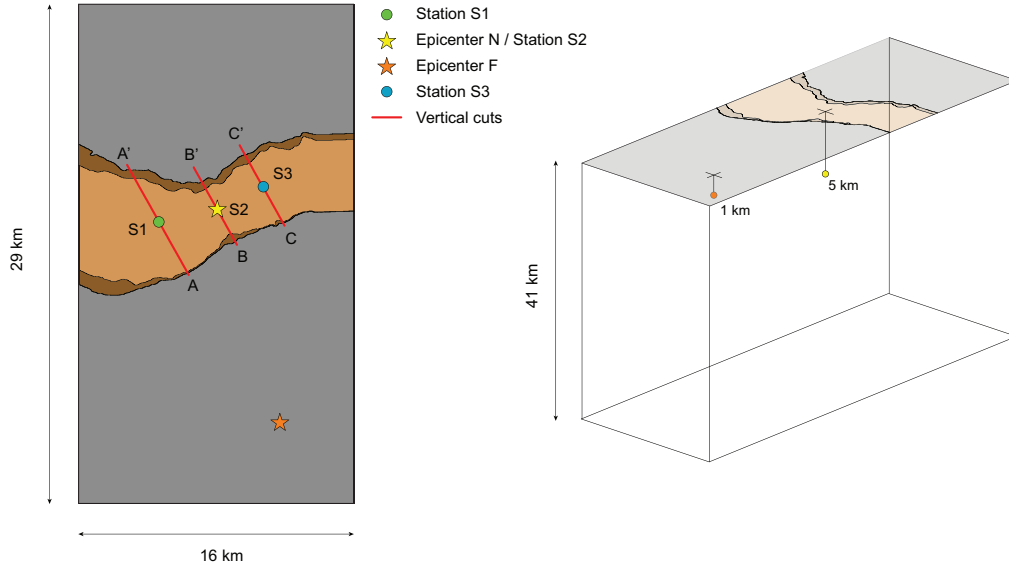


**Figure 5:** Modeling domain, location of three observation points or stations of interest, and epicenters and hypocenters of the two point sources considered for the two simulation cases. The red lines indicate the vertical cuts shown in Fig. 6 and the colors in the horizontal projection to the left match the corresponding strata characteristics.

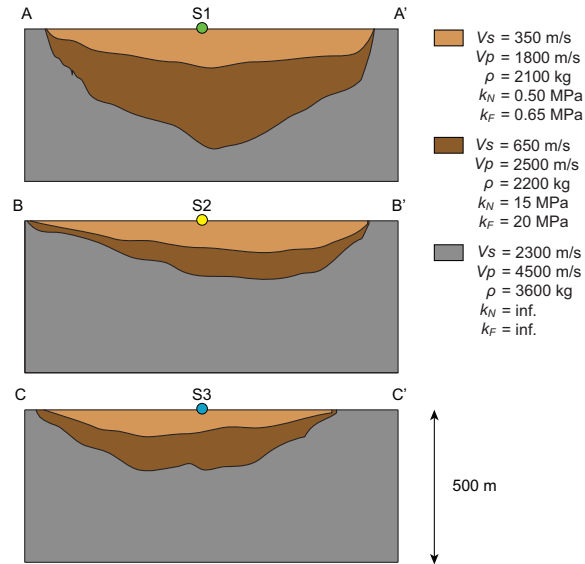


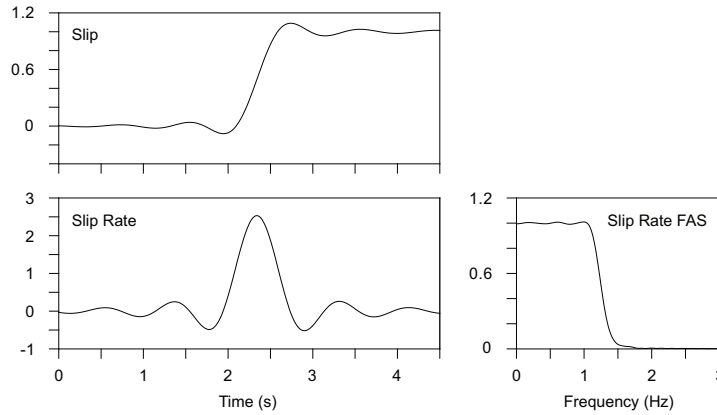
**Figure 6:** Profiles of the material model of the basin for three different vertical cuts A–A', B–B', and C–C'; and properties of each stratum.

**Table 1:** Velocity model used outside the basin.

Depth (km)	$V_p$ (m/s)	$V_s$ (m/s)	$\rho$ (kg/m <sup>3</sup> )
0–1	4500	2600	2600
1–3	6120	3420	2736
3–5	6130	3430	2744
5–7	6140	3440	2752
7–9	6150	3450	2760
9–11	6190	3480	2784
11–13	6230	3510	2808
13–15	6300	3570	2856
15–17	6420	3630	2904
17–19	6540	3700	2960
19–21	6690	3760	3008
21–23	6830	3820	3056
23–25	6970	3880	3104
25–27	7100	3940	3152
27–29	7240	4000	3200
29–31	7350	4080	3264
31–33	7460	4150	3320
33–35	7580	4240	3392
35–37	7700	4320	3456
37–41	7900	4400	3520

**Table 2:** Location and mechanism of the double-couple point sources used for the simulations.

ID	Long.	Lat.	Depth	Strike	Dip	Rake	$M_w$
N	23°17'32"	40°39'52"	5 km	260°	40°	-90°	5.3
F	23°20'06"	40°33'18"	1 km	260°	40°	-90°	5.2

**Figure 7:** Source time functions (left) and spectrum of the slip rate (right). The slip is normalized with respect to the final slip.

**Table 3:** Summary of simulation parameters and input data.

Dimensions	
Length (SN)	29320 m
Width (EW)	16160 m
Depth (UD)	40960 m
Domain coordinates*	
Southwest	23.1910, 40.5116
Northwest	23.1997, 40.7756
Northeast	23.3910, 40.7717
Southeast	23.3816, 40.5078
Projection	Bilinear
Discretization	Unstructured FE
Space	Second order
Time	Second order
Resolution	Variable
$f_{\max}$	2.0 Hz
$V_{\min}$	350 m/s
Points per wavelength	$8 \leq p < 12$
Minimum element size	20 m
Number of elements	6,683,902
Number of nodes	7,430,755
Time step $\Delta t$	0.0001 s
Simulation time	20 s

\* The corners of the domains are given in longitude and latitude

## 6 Results and Analysis

### 6.1 Regional Level

We first look at the results of the simulations from a regional perspective. Figure 8 shows the peak horizontal displacement calculated as the square root of the sum of squares of the two horizontal components of motion for the two events for the case of elastic soil conditions. We can see the differences related to the location of the sources. We, however, want to focus our attention on the response of the basin. Figure 9 shows a comparison between the elastic and elastoplastic cases for normalized horizontal displacements, velocities, and accelerations for the N-source. We have normalized the values because plasticity introduces frequencies higher than that of the excitation ( $> 1$  Hz), thus a direct comparison of amplitudes is not strictly correct. Absolute maxima are nevertheless included in each figure frame. What is of greater interest from these comparisons is how the spatial distribution of the response is affected by considering nonlinear soil conditions. Figure 10 shows the same comparison for the N-source case.

For the N-source case, the effect of considering the upper soil layers as nonlinear is immediately noticeable. In the displacements we see an increase in the response of the East side of the valley, whereas the displacements seem to decrease in most of the West part of the region. The response in the immediate vicinity the epicenter also changes considerably. In the velocities we observe a higher spatial variability, and is even higher in the accelerations. Maximum response seems to be no longer only associated to edge effects but it spreads more towards the center. For the F-source case there is less contrast because the maximum response tends to concentrate towards the South edge of the basin

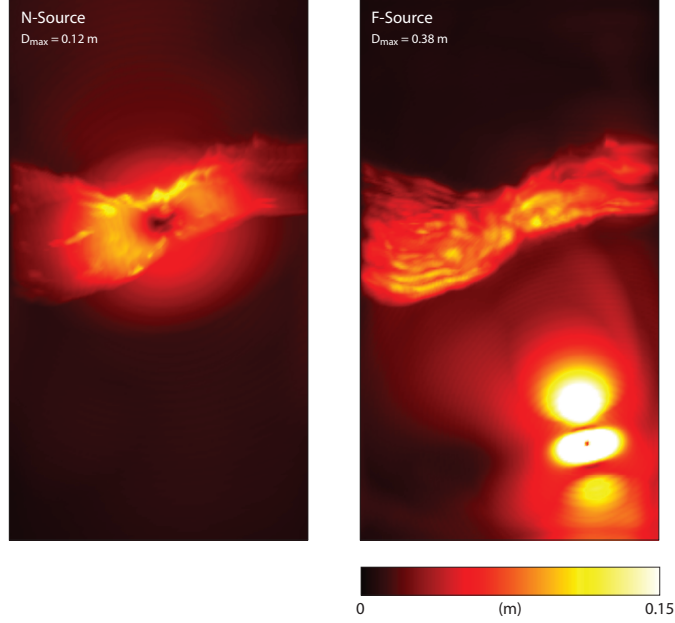


**Figure 8:** Peak horizontal displacements in the full domain for the two source cases under elastic soil conditions.

both in the elastic and the elastoplastic cases. For the displacements, higher values associated with the deeper central zones to the East and West of the central stretching arise in the nonlinear case. The same occurs with the velocities, accompanied by an increase in spatial variability. The maximum accelerations, however, seem to be more concentrated toward the South edge of the basin with two distinct clusters of higher variability to the East and West of the middle of the basin.

An alternative way to look at these results is examining the spatial variation along the lines that define the vertical cuts shown in Figs. 5 and 6. Figure 11 shows maximum displacement, velocity, and acceleration at the surface along the cut B–B' for the N-source elastic and elastoplastic simulations. At first, the fact that this comparison shows larger accelerations in the middle is at odds with the collective understanding of the effects of nonlinear soil behavior. Again, this is because in the synthetics used to extract the maxima, the elastoplastic cases have a higher energy content for frequencies larger than that of the excitation as a result of the changes from plastic flow to the elastic domain and vice versa. This does not necessarily imply that these results are invalid (because we constructed a mesh that should represent the system well up to 2 Hz). To avoid this phenomenon from affecting our interpretation we low-pass filtered the nonlinear synthetics at 1 Hz to match the frequency bandwidth of the excitation. The ‘corrected’ comparison is shown in Figs. 12–14 for the A–A', B–B', and C–C' cross sections. The corresponding comparison for the F-source case is shown in Figs. 15–17

From Figs. 12–17 we observe that the occurrence of nonlinear soil behavior affects the response of the ground for both the N- and the F-source cases. Displacements tend to be larger in the nonlinear case at points where the basin is deeper. Velocities and accelerations have a tendency to drop although in some cases may be larger than under elastic conditions. The vertical response under nonlinear conditions is lower than during the elastic for almost all points. The largest peak displacement increase is of about a factor of 3 and the largest drops in peak velocity and acceleration are of about a factor of 2.

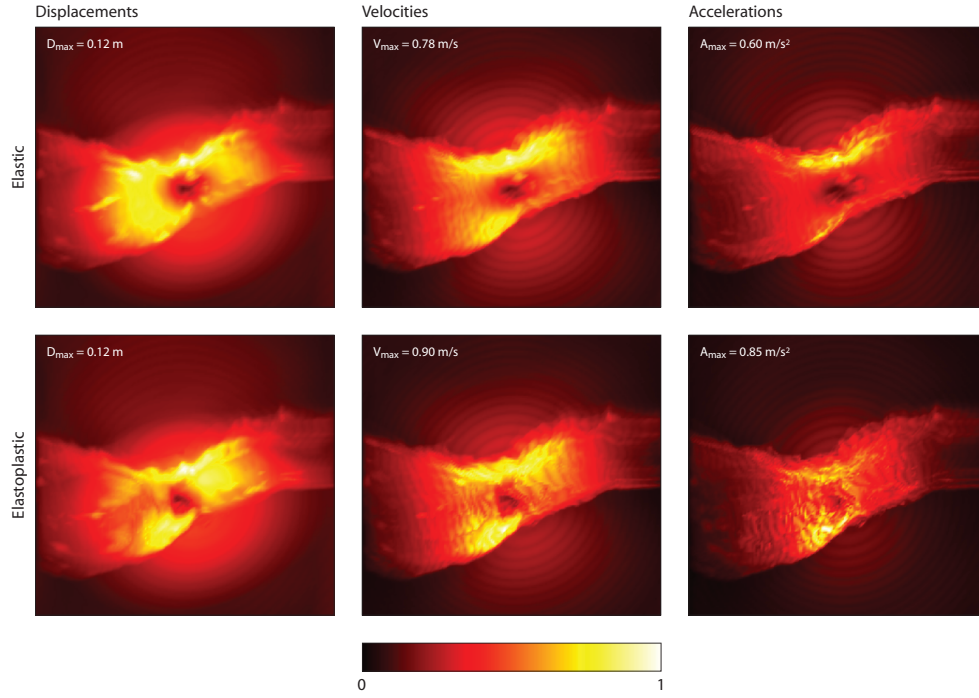


**Figure 9:** Comparison between the elastic and elastoplastic normalized peak horizontal response of the basin area for the N-source case.

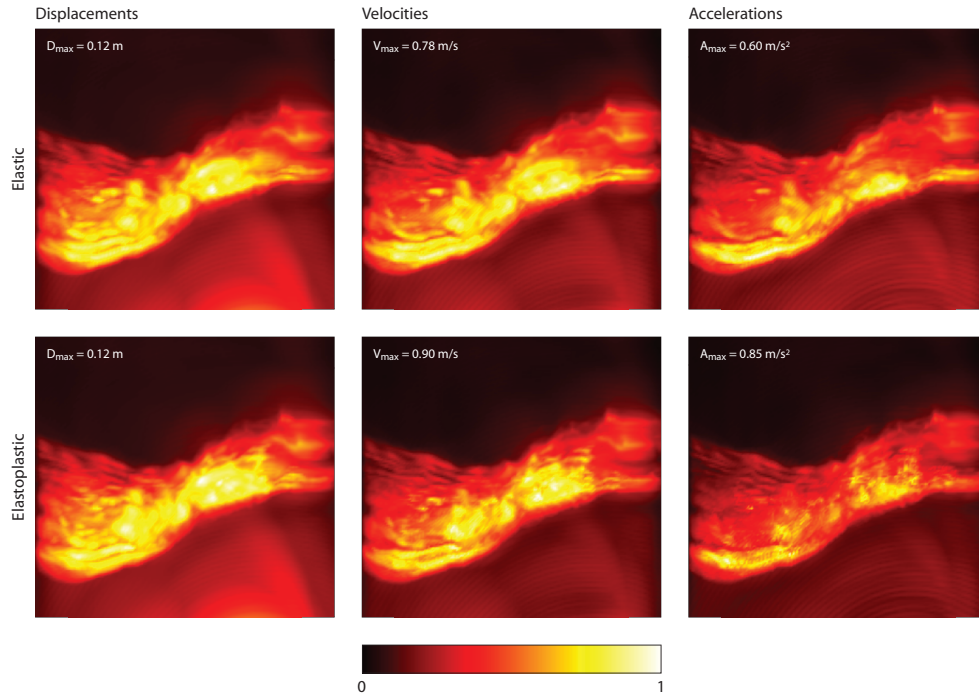


**Figure 10:** Comparison between the elastic and elastoplastic normalized peak horizontal response of the basin area for the F-source case.

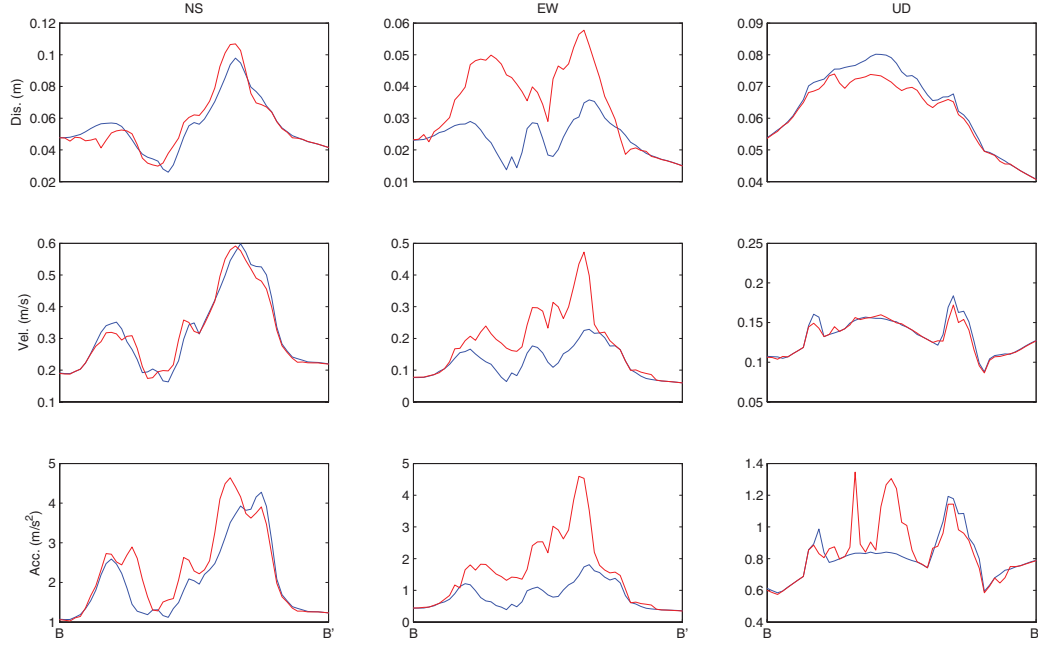


**Figure 11:** Comparison between the elastic (blue) and elastoplastic (red) maximum response at the surface along the line B–B' for the N-source case using synthetics with frequency content up to 2 Hz.

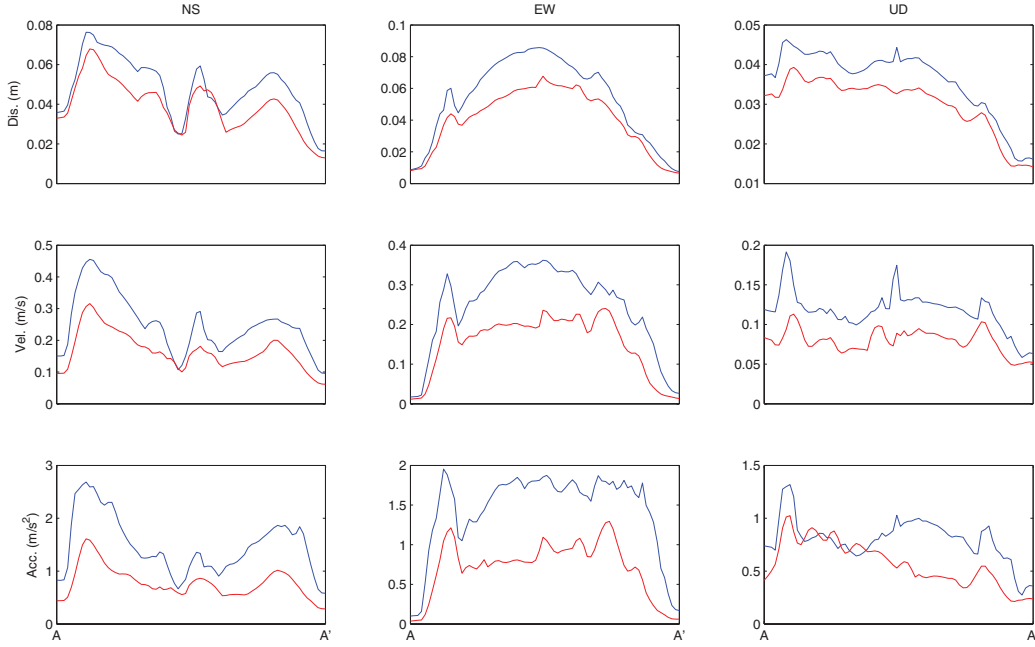


**Figure 12:** Comparison between the elastic (blue) and elastoplastic (red) maximum response at the surface along the line A–A' for the N-source case using synthetics with frequency content up to 1 Hz.

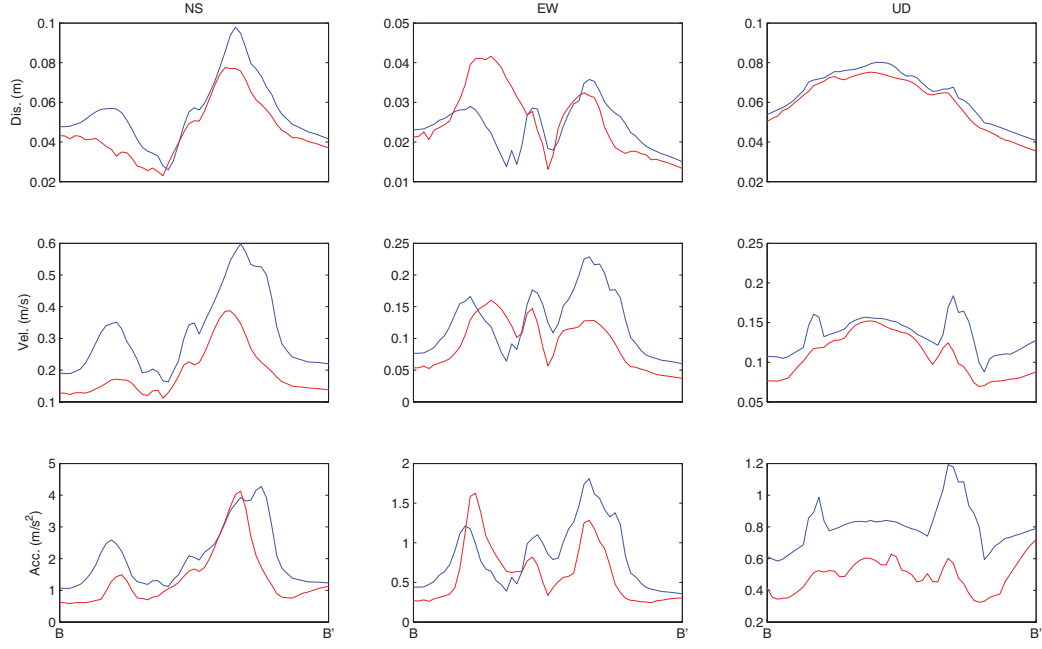


**Figure 13:** Comparison between the elastic (blue) and elastoplastic (red) maximum response at the surface along the line B–B' for the N-source case using synthetics with frequency content up to 1 Hz.

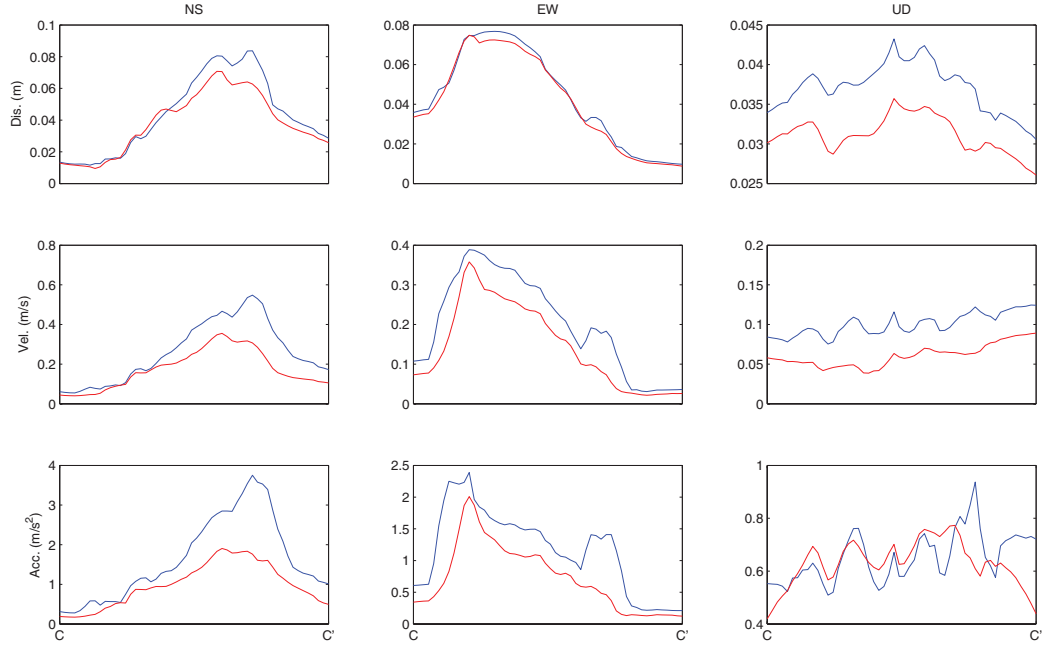


**Figure 14:** Comparison between the elastic (blue) and elastoplastic (red) maximum response at the surface along the line C–C' for the N-source case using synthetics with frequency content up to 1 Hz.



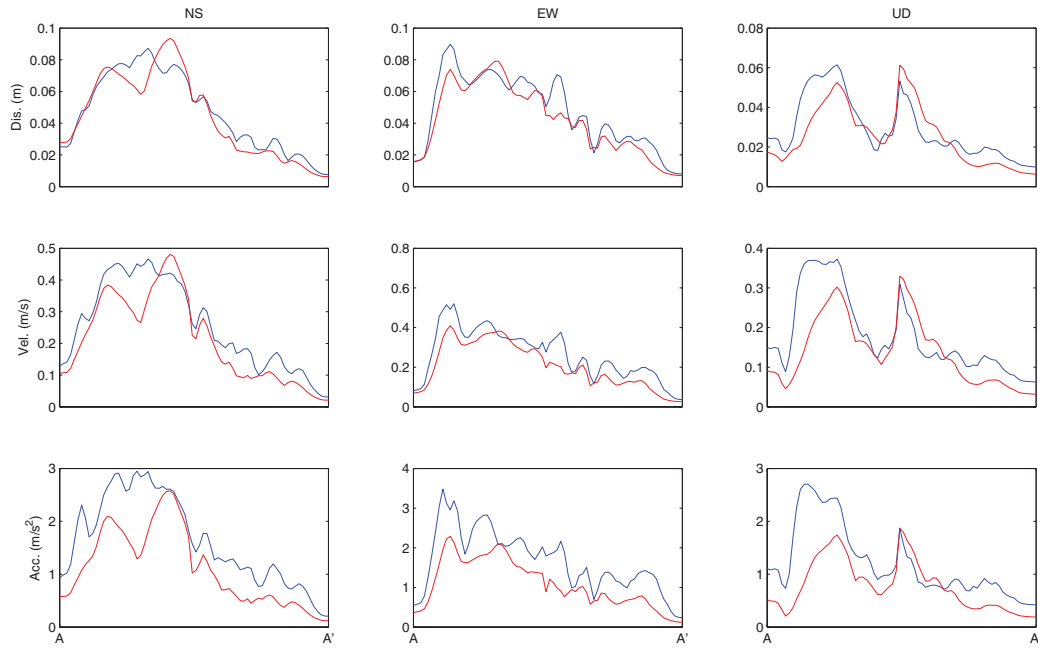


**Figure 15:** Comparison between the elastic (blue) and elastoplastic (red) maximum response at the surface along the line A–A' for the F-source case using synthetics with frequency content up to 1 Hz.

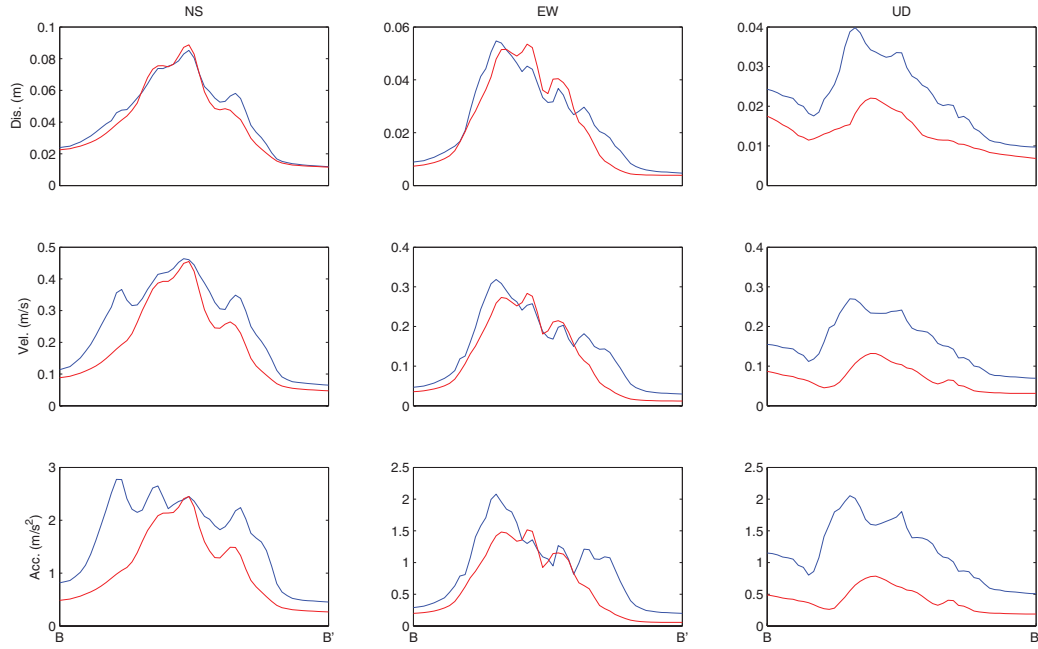


**Figure 16:** Comparison between the elastic (blue) and elastoplastic (red) maximum response at the surface along the line B–B' for the F-source case using synthetics with frequency content up to 1 Hz.

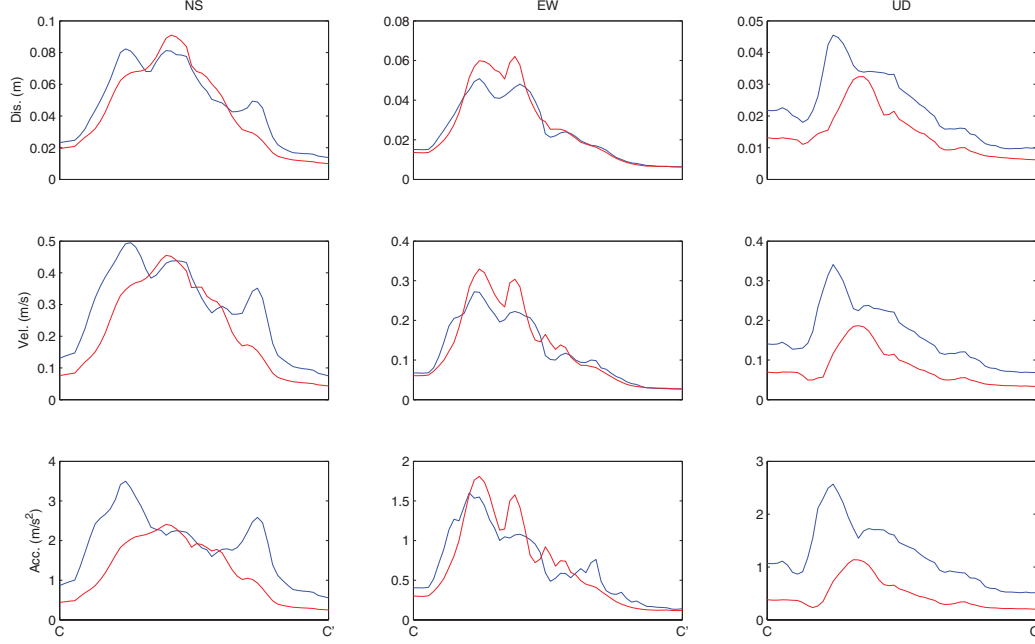


**Figure 17:** Comparison between the elastic (blue) and elastoplastic (red) maximum response at the surface along the line C–C' for the F-source case using synthetics with frequency content up to 1 Hz.

## 6.2 Local Level

Figures 18–20 depict results from the elastic and the elastoplastic cases by comparing the synthetics of stations S1, S2, and S3 for the N-source simulation. In turn, Figs. 21–23 show the corresponding results for the F-source simulation. In general, the shape of elastoplastic cases does not differ radically from that of the elastic simulation except when undergoing nonlinear deformation. Noticeable changes are well related to the time-window during which the soil at a particular location became nonlinear. For the N-source case at station S2 (Fig. 19) this happened mainly after the first wave arrival, between 1 and 4 s, indicating that plasticity occurred in association with *S*-waves. On the contrary, station S1 (Fig. 18) show changes spread through time and may have been affected by local nonlinearities associated with surface waves. The largest changes are observed at the beginning of the motion in the horizontal components of S2, and in the EW and UD components of station S1. Station S3 (Fig. 20) shows almost no change.

For the F-source case, changes are more obviously related to surface waves, as was to be expected due to the location of the excitation. In this case the largest changes are observed in stations S1 and S3, the latter experiencing more drastic changes in the EW component. In no case did we observe an effect of permanent displacement due to the nonlinear behavior. Our preliminary results suggest that this occurred because the evenly oscillatory nature of the motion due to the entrapment of waves within the valley tends to rapidly restore the motion to an elastic state, thus precluding permanent deformations. This can be seen in the EW displacement of station S2 during and after the first 5 s of the N-source simulation (Fig. 19). Further analysis will be needed to confirm this conjecture.

## 6.3 Element Level

Figs. 24 and 25 compare the elastic and elastoplastic stress-strain histories as implicit functions of time for the N- and F-source simulations, respectively; and Figs. 26 and 27 show the yield factor

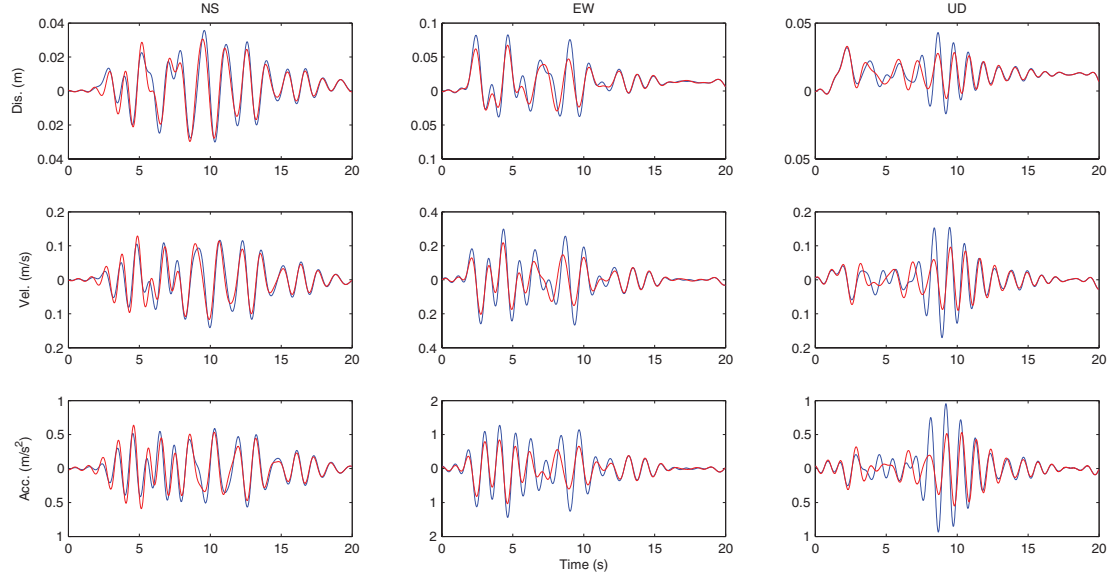


**Figure 18:** Comparison of synthetics at station S1 for the N-source case. Elastic response is shown in blue and the elastoplastic one in red. Synthetics have been low-pass filtered at 1 Hz.

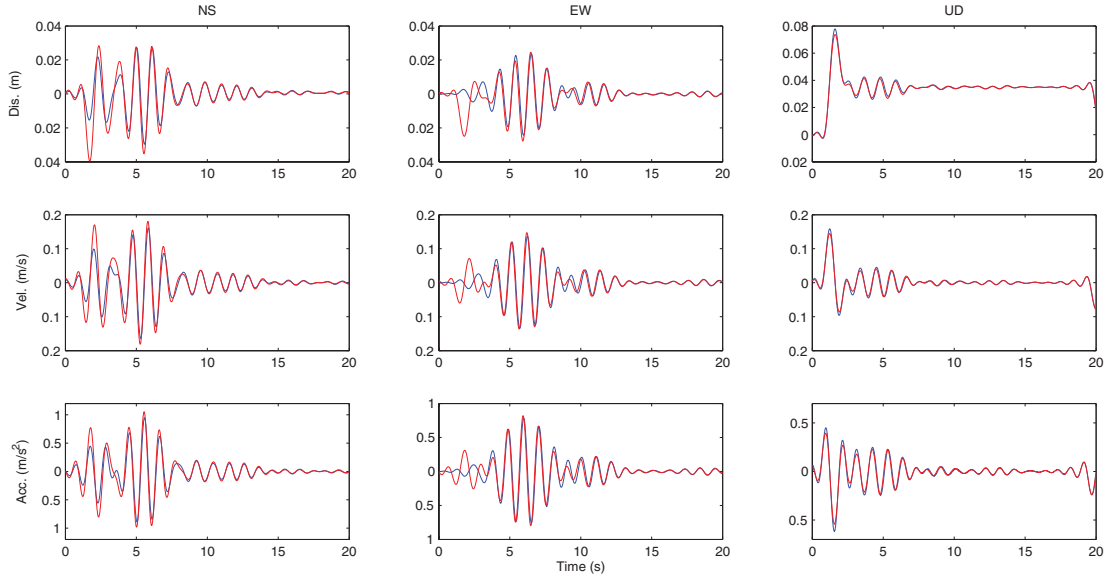


**Figure 19:** Comparison of synthetics at station S2 for the N-source case. Elastic response is shown in blue and the elastoplastic one in red. Synthetics have been low-pass filtered at 1 Hz.

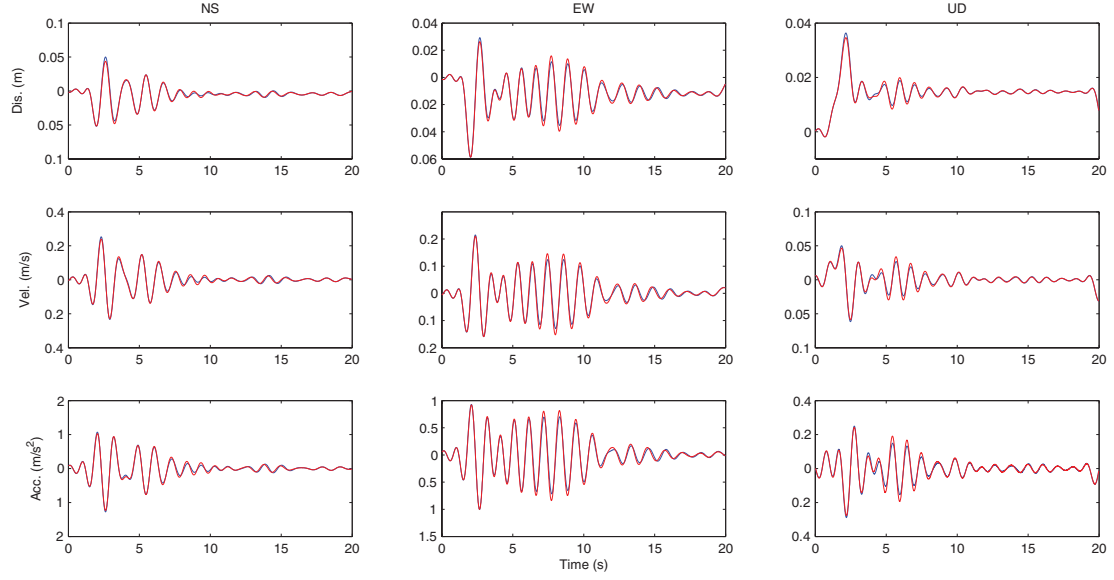


**Figure 20:** Comparison of synthetics at station S3 for the N-source case. Elastic response is shown in blue and the elastoplastic one in red. Synthetics have been low-pass filtered at 1 Hz.

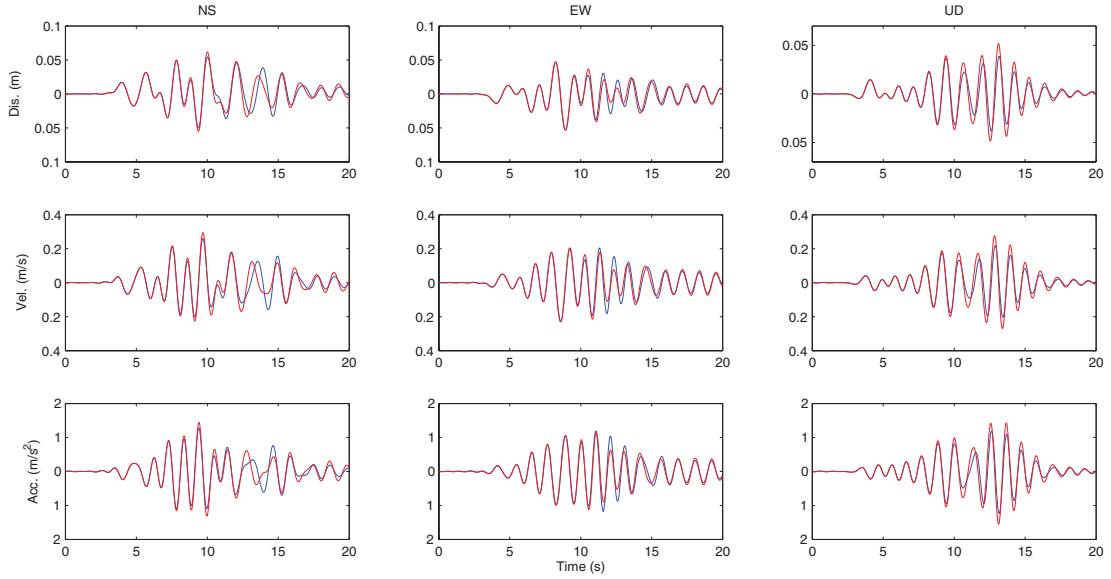


**Figure 21:** Comparison of synthetics at station S1 for the F-source case. Elastic response is shown in blue and the elastoplastic one in red. Synthetics have been low-pass filtered at 1 Hz.

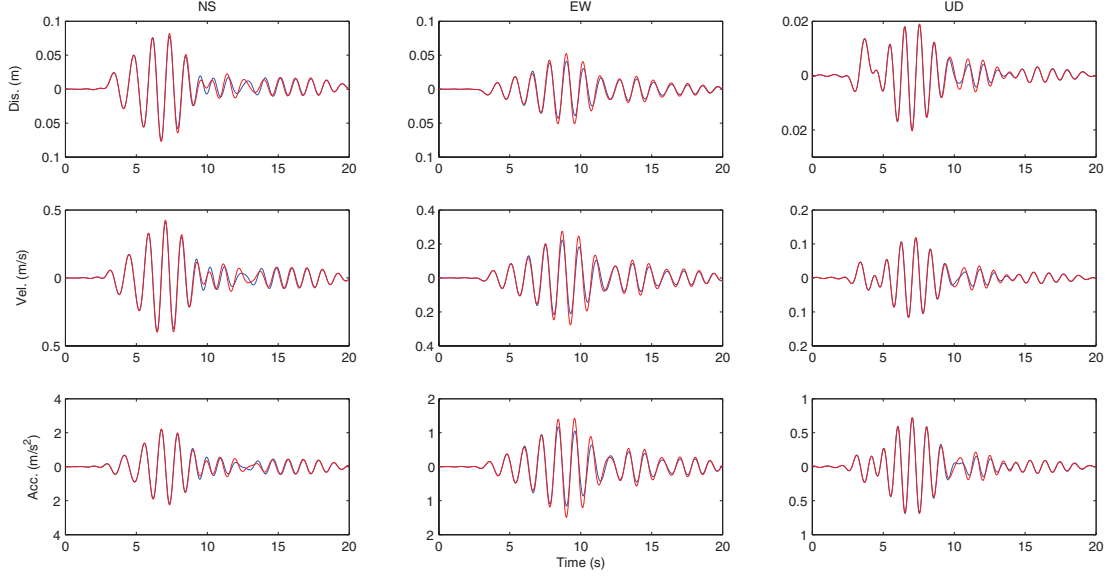


**Figure 22:** Comparison of synthetics at station S2 for the F-source case. Elastic response is shown in blue and the elastoplastic one in red. Synthetics have been low-pass filtered at 1 Hz.

$\sqrt{J_2}$  as a function of time for each source simulation. These histories were extracted from the finite elements at the free surface for stations S1, S2, and S3. We focus our attention on these curves, because having selected a von Mises material to model the soil, its inelastic behavior depends on the shear conditions derived from the second invariant of the stress deviator tensor  $J_2$ . In the figures, the axes convention is such that the SN, WE, and UD components of motion correspond to the  $x$ ,  $y$ , and  $z$  axes, respectively.

As seen from Figs. 24 and 26, at all three points in the N-source case, the inelastic deformation started near the onset of the excitation. In the S2 and S3 stations the inelastic excursions only lasted for the first few seconds of simulation but led to larger permanent strains, whereas in the S1 station the excursions into plasticity were more recurrent but produced smaller permanent strains. This results in the S2 and S3 stations experiencing larger temporal deformations. In the element containing station S3 the inelastic deformation was two-sided, with greater hysteretic energy. The same occurred for the element that contains station S1 although to a much smaller extent. By contrast, the element that contains the epicenter station S2 has a much larger inelastic deformation than the other two elements and is predominantly one-sided, although it does not experience a differential permanent deformation with respect to the elastic case. Relating the Figs. 18–20 from the previous section to Figs. 24 and 26 explains the large inelastic displacements compared to the elastic ones observed near the beginning of the excitation. Notice also the clear reduction in the maximum shear inelastic stresses with respect to the corresponding elastic ones in the element containing station S2.

By contrast, the F-source case did not produced large deformations for any of the three elements at stations S1, S2, and S3 (Figs. 25 and 27). Although all three had multiple excursions into the plastic domain, as seen in Fig. 27, none stayed long enough to cause permanent deformations. In all of them the minor inelastic behavior was two-sided (Fig. 25) and none experienced significant permanent deformation.

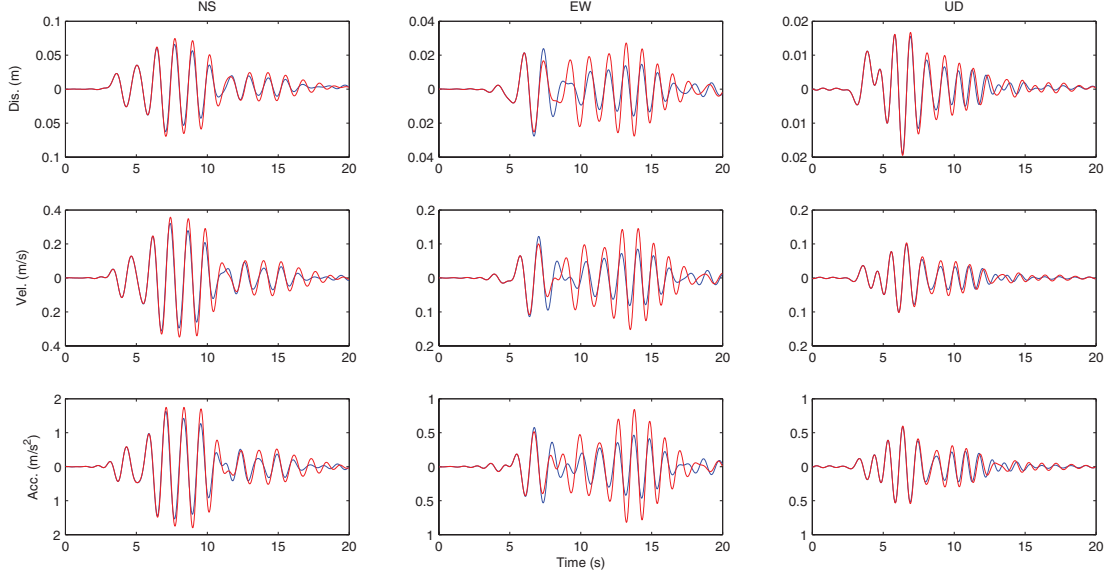


**Figure 23:** Comparison of synthetics at station S3 for the F-source case. Elastic response is shown in blue and the elastoplastic one in red. Synthetics have been low-pass filtered at 1 Hz.

## 7 Computational Performance

We now comment briefly on the computational performance of *Hercules* and its newly added implementation for nonlinear soil modeling. Table 4 shows a comparison for the statistics of two runs with characteristics like those described in Table 3, the first one under purely elastic conditions and the second one using the inelastic implementation described above. The figures in this table indicate that considering nonlinear soil conditions results in an average increase by a factor of about 2.3x the necessary time (or resources) of an equivalent simulation under elastic conditions. This is an affordable cost if one considers that, by our own estimates, for the case of anelastic ground motion simulations, *Hercules* is at least 3x faster than other large-scale earthquake simulators using finite difference approaches. In addition, a factor of 2.3x is considerably better than what may result from codes using implicit schemes for the solution of the nonlinear wave equation, for which iterative processes and convergence represent a computational burden.

## 8 Concluding Remarks

We present a formulation to incorporate nonlinear soil behavior into three-dimensional earthquake ground motion simulations in basins and describe its implementation in a finite element parallel code developed in-house for the simulation and study of the seismic response of entire regions subjected to earthquakes originated by kinematic faulting. In the present approach the inelastic semi-discretized wave equation is solved explicitly in a step-by-step manner and the solution scheme is such that it allows us to model large-scale regions efficiently.

We illustrate our implementation for a realistic basin model of a valley in the area of Thessaloniki, Greece. In this model we consider the soil in the basin to have inelastic properties that follow the behavior of a von Mises perfectly elastoplastic material. We subject the model to two point sources, one immediately below the basin at 5 km deep and the second one about 13 km to the Southeast at a depth of 1 km. Both scenarios caused the basin to behave nonlinearly, the first one causing more

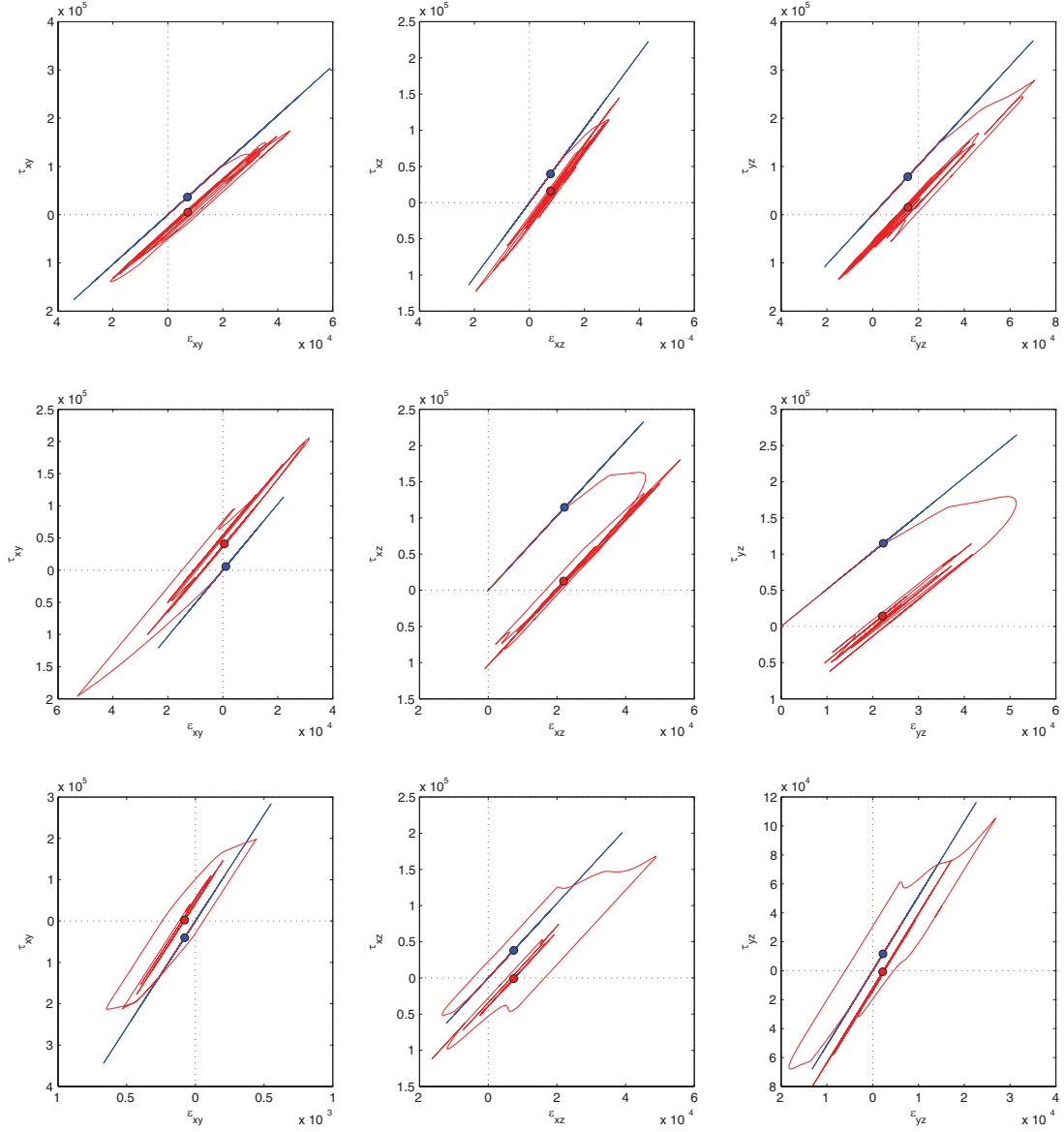


**Figure 24:** Comparison of elastic (blue) and elastoplastic (red) shear stress-strain relationship at stations S1 (top), S2 (middle), and S3 (bottom) for the N-source simulation. Filled circles indicate the final stress-strain state.

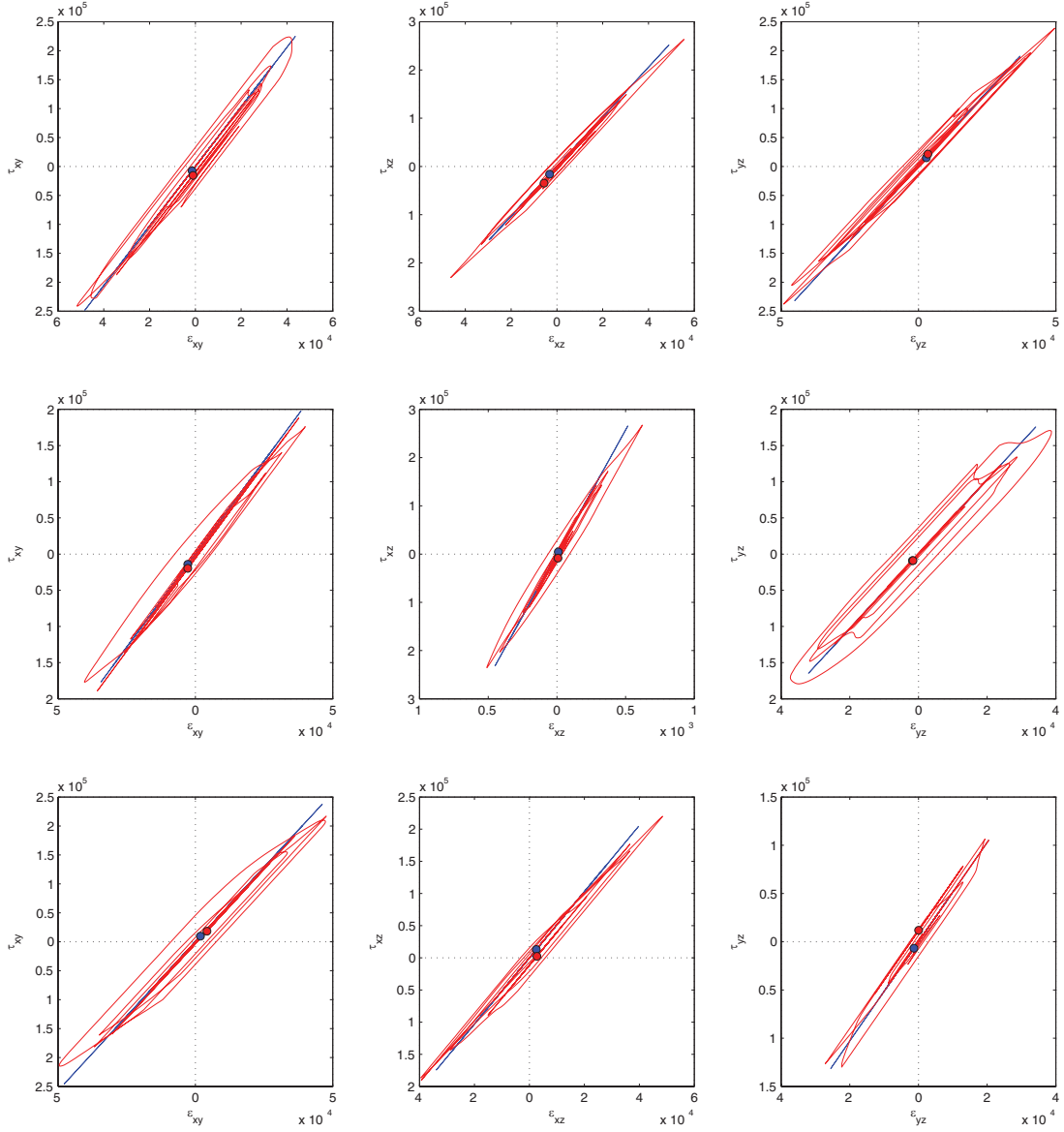


**Figure 25:** Comparison of elastic (blue) and elastoplastic (red) shear stress-strain relationship at stations S1 (top), S2 (middle), and S3 (bottom) for the F-source simulation. Filled circles indicate the final stress-strain state.



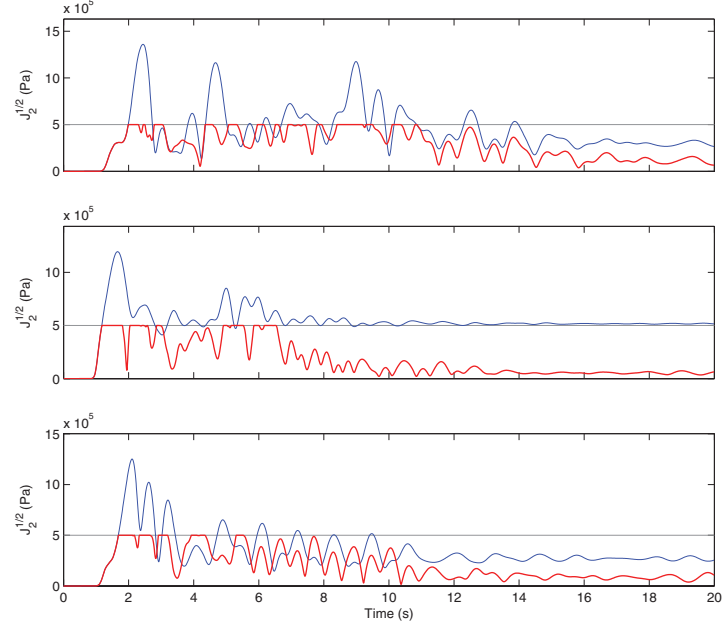


**Figure 26:** Comparison of elastic (blue) and elastoplastic (red)  $\sqrt{J_2}$  time histories at stations S1 (top), S2 (middle), and S3 (bottom) for the N-source simulation. The gray horizontal line denotes the elastic limit  $k$ .

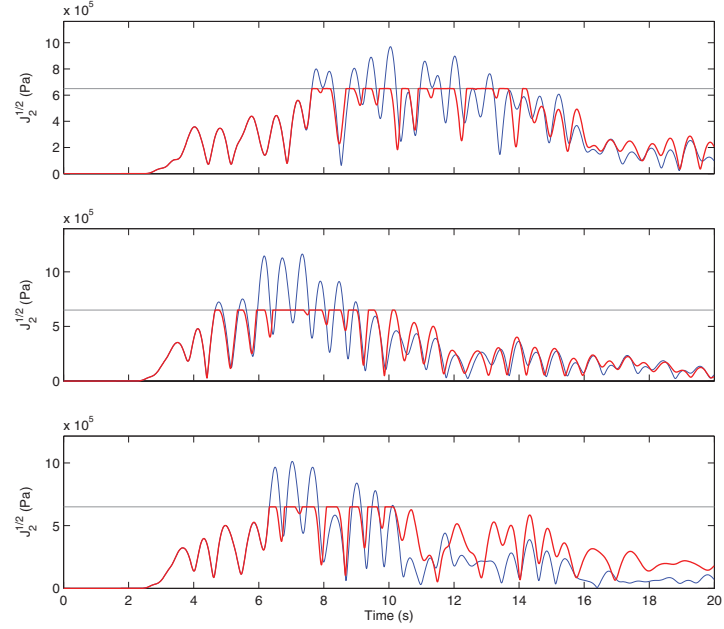


**Figure 27:** Comparison of elastic (blue) and elastoplastic (red)  $\sqrt{J_2}$  time histories at stations S1 (top), S2 (middle), and S3 (bottom) for the F-source simulation. The gray horizontal line denotes the elastic limit  $k$ .

**Table 4:** Comparison of performance statistics under elastic and inelastic conditions for two equivalent simulations.

	Elastic	Inelastic
Simulation time	20 s	20 s
Number of steps	200,000	200,000
Number of elements	6,196,584	6,683,902
Number of processors (PE)	8,192	8,192
Total running time	2,524.82 s	5,711.26 s
Meshing time	235.36 s	252.91 s
Source construction time	56.73 s	64.91 s
I/O time	1,227.11 s	2,849.92 s
Solving time	2,187.81 s	5,123.26 s
Total time/steps	0.0126 s	0.0285 s
Total time/steps/(elem./PE)	0.0000111 s	0.0000349 s

significant excursions into the plastic range associated with the arrival of early waves. The second one, although with minor nonlinear behavior, shows the nonlinear behavior to be associated with surface waves. Both cases indicate that the consideration of nonlinear soil conditions changes significantly the spatial variability of the surface ground motion due to the appearance of oscillations of frequencies larger than that of the source description. When elastic and elastoplastic cases are compared within the same frequency bands, it is observed that the inelastic behavior tends to increase the free-surface displacements whereas the velocities and accelerations may drop in some areas by up to a factor of 2.

Despite the interesting results in the present study, further analyses are necessary to understand the results this investigation and to extend them to even more realistic models of regions of interest in the United States. We plan to continue our research in this area and see it as a promising contribution to the growing field of computational seismology in the age of large parallel supercomputers.

## Acknowledgements

This research was supported by the U.S. Geological Survey (USGS), Department of the Interior, under USGS 08HQGR0018. This research was also supported by an allocation through the TeraGrid Advanced Support Program for advanced computing resources supported by the National Science Foundation. The computations were performed on BigBen at the Pittsburgh Supercomputing Center (PSC) and on Kraken at the National Institute for Computational Sciences (NICS). The views and conclusions contained in this document are those of the authors and should not be interpreted as necessarily representing the official policies, either expressed or implied, of the U.S. Government.

## References

- Abrahamson, N. A., Bolt, B. A., Darragh, R. B., Penzien, J., and Tsai, Y. B. (1987). The SMART I accelerograph array (1980-1987): A review. *Earthquake Spectra*, 3(2):263–287.
- Aki, K. (2003). A perspective on the history of strong motion seismology. *Physics of The Earth and Planetary Interiors*, 137(1-4):5–11.
- Alterman, Z. and Karal, F. C. (1968). Propagation of elastic waves in layered media by finite difference methods. *Bulletin of the Seismological Society of America*, 58(1):367–398.

- Archuleta, R. J., Bonilla, L. F., and Lavalée, D. (2000). Nonlinearity in observed and computed accelerograms. In New Zealand Society for Earthquake Engineering, editor, *Proceedings of the 12th World Conference on Earthquake Engineering*, Auckland, New Zealand. International Association for Earthquake Engineering. Paper 1934.
- Archuleta, R. J. and Day, S. M. (1980). Dynamic rupture in a layered medium: The 1966 Parkfield earthquake. *Bulletin of the Seismological Society of America*, 70(3):671–689.
- Archuleta, R. J., Liu, P., Steidl, J. H., Bonilla, L. F., Lavallée, D., and Heuzé, F. E. (2003). Finite-fault site-specific acceleration time histories that include nonlinear soil response. *Physics of The Earth and Planetary Interiors*, 137(1-4):153–181.
- Bao, H., Bielak, J., Ghattas, O., Kallivokas, L. F., O’Hallaron, D. R., Shewchuk, J. R., and Xu, J. (1996). Earthquake ground motion modeling on parallel computers. In *Proceedings of the 1996 ACM/IEEE Conference on High Performance Networking and Computing*, page 13, Pittsburgh, Pennsylvania, United States. IEEE Computer Society.
- Bao, H., Bielak, J., Ghattas, O., Kallivokas, L. F., O’Hallaron, D. R., Shewchuk, J. R., and Xu, J. (1998). Large-scale simulation of elastic wave propagation in heterogeneous media on parallel computers. *Computer Methods in Applied Mechanics and Engineering*, 152(1-2):85–102.
- Bard, P.-Y., Chaljub, E., Hollender, F., Manakou, M., and Pitilakis, K. (2008). Euroseistest numerical benchmark: Phase I. Technical report, Commissariat à l’énergie atomique (CEC), Report distributed to the participants of the Cashima-Euroseistest Benchmark.
- Bardet, J. P. and Davis, C. (1996). Engineering observations on ground motion at the Van Norman Complex after the 1994 Northridge earthquake. *Bulletin of the Seismological Society of America*, 86(1B):S333–349.
- Beresnev, I. A. (1995). Seismological evidence for nonlinear elastic ground behavior during large earthquakes. *Soil Dynamics and Earthquake Engineering*, 14(2):103–114.
- Beresnev, I. A. (2002). Nonlinearity at California generic soil sites from modeling recent strong-motion data. *Bulletin of the Seismological Society of America*, 92(2):863–870.
- Beresnev, I. A. and Wen, K.-L. (1996). Nonlinear soil response—A reality? *Bulletin of the Seismological Society of America*, 86(6):1964–1978.
- Bielak, J., Graves, R. W., Olsen, K. B., Taborda, R., Ramírez-Guzmán, L., Day, S. M., Ely, G. P., Roten, D., Jordan, T. H., Maechling, P. J., Urbanic, J., Cui, Y., and Juve, G. (2009). The Shake-Out earthquake scenario: Verification of three simulation sets. *Geophysical Journal International*. Submitted for publication.
- Bielak, J., Xu, J., and Ghattas, O. (1999). Earthquake ground motion and structural response in alluvial valleys. *Journal of Geotechnical and Geoenvironmental Engineering, ASCE*, 125(5):413–423.
- Boore, D. M. (1970). Love waves in nonuniform wave guides: Finite difference calculations. *Journal of Geophysical Research*, 75(8):1512–1527.
- Boore, D. M. (1972). *Methods in Computational Physics*, volume II, chapter Finite difference methods for seismic wave propagation in heterogeneous materials. ed. Bolt, B. A., Academic Press.
- Chang, C. Y., Power, M. S., Tang, Y. K., and Mok, C. M. (1989). Evidence of nonlinear soil response during a moderate earthquake. In *Proceedings of the 12th International Conference on Soil Mechanics and Foundation Engineering*, volume 3, pages 1927–1930, Rio de Janeiro, Brazil.

- Chen, W.-F. and Han, D.-J. (1988). *Plasticity for Structural Engineers*. Springer-Verlag, New York.
- Chin, B.-H. and Aki, K. (1991). Simultaneous study of the source, path, and site effects on strong ground motion during the 1989 loma prieta earthquake: A preliminary result on pervasive nonlinear site effects. *Bulletin of the Seismological Society of America*, 81(5):1859–1884.
- Darragh, R. B. and Shakal, A. F. (1991). The site response of two rock and soil station pairs to strong and weak ground motion. *Bulletin of the Seismological Society of America*, 81(5):1885–1899.
- Desai, C. S. and Christian, J. T. (1977). *Numerical Methods in Geotechnical Engineering*. McGraw-Hill, New York.
- Drucker, D. C. and Prager, W. (1952). Soil mechanics and plastic analysis or limit design. *Quarterly of Applied Mathematics*, 10:157–164.
- Elgamal, A., Yan, L., Yang, Z., and Conte, J. P. (2008). Three-dimensional seismic response of the Humboldt bay bridge-foundation-ground system. *Journal of Structural Engineering, ASCE*. Accepted for publication.
- Elgamal, A. W. (1991). Shear hysteretic elasto-plastic earthquake response of soil systems. *Earthquake Engineering and Structural Dynamics*, 20(4):371–387.
- Field, E. H., Johnson, P. A., Beresnev, I. A., and Zeng, Y. (1997). Nonlinear ground-motion amplification by sediments during the 1994 Northridge earthquake. *Nature*, 390(6660):599–602.
- Finn, W. D. L., Martin, G. R., and Lee, M. K. W. (1978). Comparison of dynamic analyses for saturated sands. In *Proceedings of the ASCE Geotechnical Engineering Div. Specialty Conference, Earthquake Engineering and Soil Dynamics*, ASCE, pages 472–491, Pasadena, CA.
- Frankel, A. and Stephenson, W. (2000). Three-dimensional simulations of ground motions in the Seattle region for earthquakes in the Seattle fault zone. *Bulletin of the Seismological Society of America*, 90(5):1251–1267.
- Frankel, A. and Vidale, J. (1992). A three-dimensional simulation of seismic waves in the Santa Clara Valley, California, from a Loma Prieta aftershock. *Bulletin of the Seismological Society of America*, 82(5):2045–2074.
- Frankel, A. D., Carver, D. L., and Williams, R. A. (2002). Nonlinear and linear site response and basin effects in Seattle for the  $M$  6.8 Nisqually, Washington, earthquake. *Bulletin of the Seismological Society of America*, 92(6):2090–2109.
- Fung, Y. C. (1965). *Foundations of Solid Mechanics*. Prentice Hall, Inc.
- Furumura, T. and Koketsu, K. (2000). Parallel 3-d simulation of ground motion for the 1995 Kobe earthquake: The component decomposition approach. *Pure and Applied Geophysics*, 157(11-12):2047–2062.
- Graves, R. W. (1996). Simulating seismic wave propagation in 3D elastic media using staggered-grid finite differences. *Bulletin of the Seismological Society of America*, 86(4):1091–1106.
- Graves, R. W. (1998). Three-dimensional finite-difference modeling of the san andreas fault: Source parameterization and ground-motion levels. *Bulletin of the Seismological Society of America*, 88(4):881–897.
- Graves, R. W., Aagaard, B. T., Hudnut, K., Star, L. M., Stewart, J. P., and Jordan, T. H. (2008). Broadband simulations for  $M_w$  7.8 southern San Andreas earthquakes: ground motion sensitivity to rupture speed. *Geophysical Research Letters*, 35:L22302.

- Hardin, B. O. and Drnevich, V. P. (1972). Shear modulus and damping in soils: Measurement and parameters effects. *Journal of the Soil Mechanics and Foundations Division, ASCE*, 98(SM6):603–624. Paper 8977.
- Hartzell, S., Leeds, A., Frankel, A., Williams, R. A., Odum, J., Stephenson, W., and Silva, W. (2002). Simulation of broadband ground motion including nonlinear soil effects for a magnitude 6.5 earthquake on the Seattle Fault, Seattle, Washington. *Bulletin of the Seismological Society of America*, 92(2):831–853.
- Idriss, I. M. and Seed, H. B. (1968). Seismic response of horizontal soil layers. *Journal of the Soil Mechanics and Foundations Division, ASCE*, 94(SM4):1003–1031.
- Jones, L. M., Bernknopf, R., Cox, D., Goltz, J., Hudnut, K., Mileti, D., Perry, S., Ponti, D., Porter, K., Reichle, M., Seligson, H., Shoaf, K., Treiman, J., and Wein, A. (2008). The ShakeOut scenario. Technical Report USGS-R1150, CGS-P25, U.S. Geological Survey and California Geological Survey.
- Joyner, W. B. (1975). A method for calculating nonlinear seismic response in two dimensions. *Bulletin of the Seismological Society of America*, 65(5):1337–1357.
- Joyner, W. B. and Chen, A. T. F. (1975). Calculation of nonlinear ground response in earthquakes. *Bulletin of the Seismological Society of America*, 65(5):1315–1336.
- Käser, M. and Dumbser, M. (2006). An arbitrary high-order discontinuous galerkin method for elastic waves on unstructured meshes — I. The two-dimensional isotropic case with external source terms. *Geophysical Journal International*, 166(2):855–877.
- Käser, M. and Gallovic, F. (2008). Effects of complicated 3D rupture geometries on earthquake ground motion and their implications: A numerical study. *Geophysical Journal International*, 172(1):276–292.
- Kelly, K. R., Ward, R. W., Treitel, S., and Alford, R. M. (1976). Synthetic seismograms: A finite-difference approach. *Geophysics*, 41(1):2–27.
- Kim, E. J., Bielak, J., and Ghattas, O. (2003). Large-scale Northridge earthquake simulation using octree-based multiresolution mesh method. In *Proceedings of the 16th ASCE Engineering Mechanics Conference*, Seattle, Washington. University of Washington.
- Komatitsch, D., Liu, Q., Tromp, J., Suss, P., Stidham, C., and Shaw, J. H. (2004). Simulations of ground motion in the Los Angeles basin based upon the spectral-element method. *Bulletin of the Seismological Society of America*, 94(1):187–206.
- Komatitsch, D. and Vilotte, J.-P. (1998). The spectral element method: An efficient tool to simulate the seismic response of 2D and 3D geological structures. *Bulletin of the Seismological Society of America*, 88(2):368–392.
- Lysmer, J. and Drake, L. A. (1972). A finite element method for seismology. In Alder, B., Fernbach, S., and Bolt, B., editors, *Methods in Computational Physics*, volume 11, chapter 6. Academic Press, New York.
- Lysmer, J. and Kuhlemeyer, R. L. (1969). Finite dynamic model for infinite media. *Journal of the Engineering Mechanics Division, ASCE*, 95(EM4):859–877.
- Marsh, J., Larkin, T. J., Haines, A. J., and Benites, R. A. (1995). Comparison of linear and nonlinear seismic responses of two-dimensional alluvial basins. *Bulletin of the Seismological Society of America*, 85(3):874–889.

- Olsen, K. B., Archuleta, R. J., and Matarese, J. R. (1995a). Three-dimensional simulation of a magnitude 7.75 earthquake on the san andreas fault. *Science*, 270(5242):1628–1632.
- Olsen, K. B., Day, S. M., Dalaguer, L. A., Mayhew, J., Cui, Y., Zhu, J., Cruz-Atienza, V. M., Roten, D., Maechling, P., Jordan, T. H., Okaya, D., and Chourasia, A. (2009). Shakeout-d: Ground motion estimates using an ensemble of large earthquakes on the southern san andreas fault with spontaneous rupture propagation. *Geophysical Research Letters*. In Press.
- Olsen, K. B., Day, S. M., Minster, J. B., Cui, Y., Chourasia, A., Faerman, M., Moore, R., Maechling, P., and Jordan, T. (2006). Strong shaking in los angeles expected from southern san andreas earthquake. *Geophysical Research Letters*, 33(L07305):1–4.
- Olsen, K. B., Day, S. M., Minster, J. B., Cui, Y., Chourasia, A., Okaya, D., Maechling, P., and Jordan, T. (2008). Terashake2: Spontaneous rupture simulations of  $M_W$  7.7 earthquakes on the southern San Andreas fault. *Bulletin of the Seismological Society of America*, 98(3):1162–1185.
- Olsen, K. B., Pechmann, J. C., and Schuster, G. T. (1995b). Simulation of 3D elastic wave propagation in the Salt Lake basin. *Bulletin of the Seismological Society of America*, 85(6):1688–1710.
- Papazachos, C. B. (1998). Crustal  $p$ - and  $s$ -velocity structure of the Serbomacedonian Massif (Northern Greece) obtained by non-linear inversion of traveltimes. *Geophysical Journal International*, 134(1):25–39.
- Pitarka, A., Irikura, K., Iwata, T., and Sekiguchi, H. (1998). Three-dimensional simulation of the near-fault ground motion for the 1995 Hyogo-Ken Nanbu (Kobe), Japan, earthquake. *Bulletin of the Seismological Society of America*, 88(2):428–440.
- Pitilakis, K. (2008). Euroseistest report for the cashima project. Technical report, Department of Civil Engineering, Aristotle University of Thessaloniki, Greece, Report distributed to the participants of the Cashima-Euroseistest Benchmark.
- Ramírez-Guzmán, L., Contreras, M., Taborda, R., and Bielak, J. (2008). Ground motion in the valley of Mexico: Basin effects. In *SSA Annual Meeting, Santa Fe, NM, USA, April 16–18*.
- Raptakis, D., Chávez-García, F. J., Makra, K., and Pitilakis, K. (2000). Site effects at Euroseistest–I. Determination of the valley structure and confrontation of observations with 1D analysis. *Soil Dynamics and Earthquake Engineering*, 19(1):1–2.
- Raptakis, D., Theodulidis, N., and Pitilakis, K. (1998). Data analysis of the Euroseistest strong motion array in Volvi (Greece): Standard and horizontal-to-vertical spectral ratio techniques. *Earthquake Spectra*, 14(1):203–224.
- Rubinstein, J. L. and Beroza, G. C. (2004a). Evidence for widespread nonlinear strong ground motion in the  $M_W$  6.9 Loma Prieta earthquake. *Bulletin of the Seismological Society of America*, 94(5):1595–1608.
- Rubinstein, J. L. and Beroza, G. C. (2004b). Nonlinear strong ground motion in the  $M_L$  5.4 Chittenden earthquake: Evidence that preexisting damage increases susceptibility to further damage. *Geophysical Research Letters*, 31(23):L23614.1–4.
- Rubinstein, J. L., Uchida, N., and Beroza, G. C. (2007). Seismic velocity reductions caused by the 2003 Tokachi-Oki earthquake. *Journal of Geophysical Research*, 112(B11):B05315.
- Satoh, T., Sato, T., and Kawase, H. (1995). Nonlinear behavior of soil sediments identified by using borehole records observed at the Ashigra Valley, Japan. *Bulletin of the Seismological Society of America*, 85(6):1821–1834.

- Schaff, D. P. and Beroza, G. C. (2004). Coseismic and postseismic velocity changes measured by repeating earthquakes. *Journal of Geophysical Research*, 109(B10):B10302.
- Seed, H. B. and Idriss, I. M. (1969). Influence of soil condition on ground motions during earthquakes. *Journal of the Soil Mechanics and Foundations Division, ASCE*, 95(SM1):99–137. Paper 6347.
- Semblat, J. F., Kham, M., Parara, E., Bard, P.-Y., Pitilakis, K., Makra, K., and Raptakis, D. (2005). Seismic wave amplification: Basin geometry vs soil layering. *Soil Dynamics and Earthquake Engineering*, 25(7–10):529–538.
- Seriani, G. (1998). 3-D large-scale wave propagation modeling by spectral element method on Cray T3E multiprocessor. *Computer Methods in Applied Mechanics and Engineering*, 64(1–2):235–247.
- Seriani, G. and Priolo, E. (1994). Spectral element method for acoustic wave simulation in heterogeneous media. *Finite Elements in Analysis and Design*, 16(3–4):337–348.
- Streeter, V. L., Wylie, E. B., and Richart, F. E. (1974). Soil motion computations by characteristics method. *Journal of the Geotechnical Engineering Division, ASCE*, 100(3):247–263.
- Taborda, R., Ramírez-Guzmán, L., López, J., Urbanic, J., Bielak, J., and O’Hallaron, D. (2007). ShakeOut and its effects in Los Angeles and Oxnard areas. *Eos Transcripts of the American Geophysical Union*, 88(52): Fall Meeting Supplement, Abstract IN21B–0477.
- Taborda, R., Ramírez-Guzmán, L., Tu, T., Kim, E. J., López, J., Bielak, J., Ghattas, O., and O’Hallaron, D. (2006). Scaling up TeraShake: A 1-Hz case study. *Eos Transcripts of the American Geophysical Union*, 87(52): Fall Meeting Supplement, Abstract S51E–07.
- Trifunac, M. D. and Todorovska, M. I. (1996). Nonlinear soil response—1994 Northridge, California, Earthquake. *Journal of Geotechnical Engineering, ASCE*, 122(9):725–735.
- Tsuda, K., Steidl, J., Archuleta, R., and Assimaki, D. (2006). Site-response estimation for the 2003 Miyagi-Oki earthquake sequence considering nonlinear site response. *Bulletin of the Seismological Society of America*, 96(4A):1474–1482.
- Tu, T., Yu, H., Ramírez-Guzmán, L., Bielak, J., Ghattas, O., Ma, K.-L., and O’Hallaron, D. R. (2006a). From mesh generation to scientific visualization: An end-to-end approach to parallel supercomputing. In *Proceedings of the 2006 ACM/IEEE International Conference for High Performance Computing, Networking, Storage and Analysis*, page 15, Tampa, Florida. IEEE Computer Society.
- Tu, T., Yu, H., Ramírez-Guzmán, L., Bielak, J., Ghattas, O., Ma, K.-L., and O’Hallaron, D. R. (2006b). From physical modeling to scientific understanding — An end-to-end approach to parallel supercomputing. Technical Report CMU-CS-06-105, School of Computer Science, Carnegie Mellon University, Pittsburgh, Pennsylvania.
- Wen, K.-L. (1994). Non-linear soil response in ground motions. *Earthquake Engineering and Structural Dynamics*, 23(6):599–608.
- Xu, J. (1998). *Three dimensional simulation of wave propagation in inelastic media on parallel computers*. PhD thesis, Carnegie Mellon University.
- Xu, J., Bielak, J., Ghattas, O., and Wang, J. (2003). Three-dimensional nonlinear seismic ground motion modeling in basins. *Physics of The Earth and Planetary Interiors*, 137(1-4):81–95.
- Yan, L. (2006). *Sensor data analysis and information extraction for structural health monitoring, Appendices A and B: Three-dimensional bridge-foundation-ground system, computational model and seismic response*. PhD thesis, University of California, San Diego.

- Yang, Z., He, L., Bielak, J., Zhang, Y., Elgamal, A., and Conte, J. P. (2003). Nonlinear seismic response of a bridge site subjected to spatially varying ground motion. In *Proceedings of the 16th ASCE Engineering Mechanics Conference*, Seattle, Washington. University of Washington.
- Yu, G., Anderson, J. G., and Siddharthan, R. (1993). On the characteristics of nonlinear soil response. *Bulletin of the Seismological Society of America*, 83(1):218–244.
- Zhang, B. and Papageorgiou, A. S. (1996). Simulation of the response of the Marina District Basin, San Francisco, California, to the 1989 Loma Prieta earthquake. *Bulletin of the Seismological Society of America*, 86(5):1382–1400.
- Zhang, Y., Acero, G., Conte, J. P., Yang, Z., and Elgamal, A. (2004). Seismic reliability assesment of a bridge ground system. In Canadian Association for Earthquake Engineering, editor, *Proceedings of the 13th World Conference on Earthquake Engineering*, Vancouver, British Columbia, Canada. International Association for Earthquake Engineering. Paper 2978.
- Zhang, Y., Conte, J. P., Yang, Z., Elgamal, A., Bielak, J., and Acero, G. (2008). Two-dimensional nonlinear earthquake response analysis of a bridge-foundation-ground system. *Earthquake Spectra*, 24(2):343–386.
- Zhang, Y., Yang, Z., Bielak, J., Conte, J. P., and Elgamal, A. (2003). Treatment of seismic input and boundary conditions in nonlinear seismic analysis of a bridge ground system. In *Proceedings of the 16th ASCE Engineering Mechanics Conference*, Seattle, Washington. University of Washington.